

AD-A110 836

STEVENS INST OF TECH· HOBOKEN NJ DAVIDSON LAB

F/8 20/4

CORRELATION OF THEORETICAL PREDICTIONS OF PROPELLER-INDUCED MUL--ETC(U)

NOV 80 S TSAKONAS, J P BRESLIN, J TEETERS

N00014-79-C-0240

NL

UNCLASSIFIED

SIT-DL-80-9-2140

1-1
PAGE 10

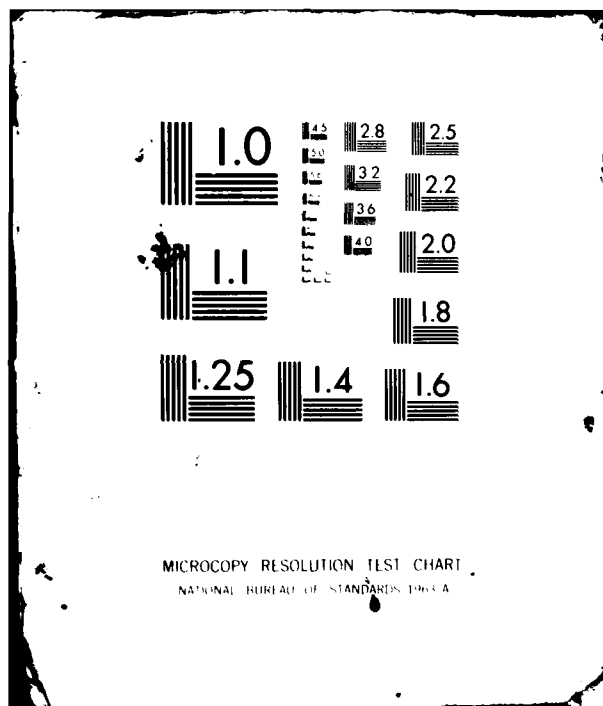
END

DATE

FILED

3 82

DTIC



AD A110836

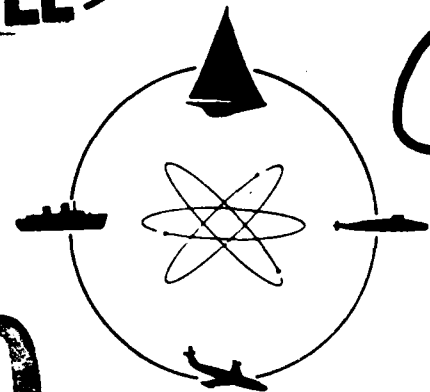


STEVENS INSTITUTE
OF TECHNOLOGY

CASTLE POINT STATION
HOBOKEN, NEW JERSEY 07030

LEVEL II

R-2140



TIC
ECTE
B 11 1982

D

E

DAVIDSON LABORATORY

Report SIT-DL-80-9-2140

November 1980

CORRELATION OF THEORETICAL PREDICTIONS
OF PROPELLER-INDUCED HULL PRESSURES
WITH AVAILABLE DATA

by

S. Tsakonas, J.P. Breslin, and J. Teeters

APPROVED FOR PUBLIC RELEASE
DISTRIBUTION UNLIMITED

This study is sponsored by the
Naval Sea Systems Command
General Hydromechanics Research Program
Administered by the
David W. Taylor
Naval Ship Research & Development Center
Under

Contract N00014-79-C-0240
DL Project 057/4704

R-2140

8 2 0 2 1 0 0 8 7

UNCLASSIFIED

SECURITY CLASSIFICATION OF THIS PAGE (When Data Entered)

REPORT DOCUMENTATION PAGE		READ INSTRUCTIONS BEFORE COMPLETING FORM
1. REPORT NUMBER Report SIT-DL-80-9-2140	2. GOVT ACCESSION NO. AD-A110 836	3. RECIPIENT'S CATALOG NUMBER
4. TITLE (and Subtitle) CORRELATION OF THEORETICAL PREDICTIONS OF PROPELLER-INDUCED HULL PRESSURES WITH AVAILABLE DATA.		5. TYPE OF REPORT & PERIOD COVERED FINAL
		6. PERFORMING ORG. REPORT NUMBER
7. AUTHOR(s) S. Tsakonas J.P. Breslin J. Teeters		8. CONTRACT OR GRANT NUMBER(s) N00014-79-C-0240
9. PERFORMING ORGANIZATION NAME AND ADDRESS Davidson Laboratory Stevens Institute of Technology Castle Point Station, Hoboken, NJ 07030		10. PROGRAM ELEMENT, PROJECT, TASK AREA & WORK UNIT NUMBERS 61153N R02301 SR 023 01 01
11. CONTROLLING OFFICE NAME AND ADDRESS DAVID W. TAYLOR NAVAL SHIP RESEARCH AND DEVELOPMENT CENTER, Code 1505 Bethesda, MD 20084		12. REPORT DATE November 1980
		13. NUMBER OF PAGES viii+42 pp. + 11 figures
14. MONITORING AGENCY NAME & ADDRESS (if different from Controlling Office) OFFICE OF NAVAL RESEARCH 800 N. Quincy Street Arlington, VA 22217		15. SECURITY CLASS. (of this report) UNCLASSIFIED
		15a. DECLASSIFICATION/DOWNGRADING SCHEDULE
16. DISTRIBUTION STATEMENT (of this Report) APPROVED FOR PUBLIC RELEASE; DISTRIBUTION UNLIMITED		
17. DISTRIBUTION STATEMENT (of the abstract entered in Block 20, if different from Report)		
18. SUPPLEMENTARY NOTES Sponsored by the Naval Sea Systems Command, General Hydromechanics Research Program; Administered by the David W. Taylor Naval Ship Research and Development Center, Code 1505, Bethesda, MD 20084.		
19. KEY WORDS (Continue on reverse side if necessary and identify by block number) Propeller-induced Point Pressures.		
20. ABSTRACT (Continue on reverse side if necessary and identify by block number) A method has been developed to calculate the blade frequency point pressure on a hull surface in the presence of a propeller and a free water surface. The approach is based on that previously employed in calculating the propeller-induced hull forces (Ref 3) in which the hull is represented by a source distribution smeared over the hull surface whose strength is determined through the solution of a Fredholm integral equation of the 2nd kind in terms of specified propeller-induced velocities. Point pressures (Continued)		

DD FORM 1 JAN 73 1473

EDITION OF 1 NOV 65 IS OBSOLETE
S/N 0102-014-6601

UNCLASSIFIED

SECURITY CLASSIFICATION OF THIS PAGE (When Data Entered)

UNCLASSIFIED

SECURITY CLASSIFICATION OF THIS PAGE(When Data Entered)

20. Abstract (Continued)

are determined by superposing the free-space pressure emanating from the propeller through its fanning action on the pressure due to the diffraction potential. A series of calculations was performed for the case of a model tanker tested extensively at the Norwegian Experimental Tank (Ship and Ocean Laboratory, Norwegian Hydrodynamic Laboratories, Marine Technology Center). The agreement between experimental and predicted values varies from point to point; in general, the maximum deviation of amplitude is between $\pm 30\%$, but the phases are in poor agreement. A new method is suggested in which the hull is represented by a doublet distribution rather than a source distribution. This approach which reduces computing time considerably permits improved accuracy and results in much better correlation between experimental and calculated values.

4

UNCLASSIFIED

SECURITY CLASSIFICATION OF THIS PAGE(When Data Entered)

STEVENS INSTITUTE OF TECHNOLOGY
DAVIDSON LABORATORY
CASTLE POINT STATION
HOBOKEN, NEW JERSEY

Report SIT-DL-80-9-2140

November 1980

Accession For	
NTIS GRA&I	<input checked="" type="checkbox"/>
DTIC TAB	<input type="checkbox"/>
Unannounced	<input type="checkbox"/>
Justification	<input type="checkbox"/>
By _____	
Distribution/	
Availability Codes	
Dist	Avail and/or Special
A	

CORRELATION OF THEORETICAL PREDICTIONS
OF PROPELLER-INDUCED HULL PRESSURES WITH AVAILABLE DATA

by


S. Tsakonas, J.P. Breslin, and J. Teeters

This study was sponsored by the
Naval Sea Systems Command
General Hydromechanics Research Program
Administered by the
David W. Taylor Naval Ship Research & Development Center
Under
Contract N00014-79-C-0240
DL Project 057/4704

APPROVED FOR PUBLIC RELEASE
DISTRIBUTION UNLIMITED

viii+42 pp. +11 figures

Approved:


John P. Breslin
Director

ABSTRACT

A method has been developed to calculate the blade frequency point pressure on a hull surface in the presence of a propeller and a free water surface. The approach is based on that previously employed in calculating the propeller-induced hull forces⁽³⁾ in which the hull is represented by a source distribution smeared over the hull surface whose strength is determined through the solution of a Fredholm integral equation of the 2nd kind in terms of specified propeller-induced velocities. Point pressures are determined by superposing the free-space pressure emanating from the propeller through its fanning action on the pressure due to the diffraction potential. A series of calculations was performed for the case of a model tanker tested extensively at the Norwegian Experimental Tank (Ship and Ocean Laboratory, Norwegian Hydrodynamic Laboratories, Marine Technology Center). The agreement between experimental and predicted values varies from point to point; in general, the maximum deviation of amplitude is between $\pm 30\%$, but the phases are in poor agreement. A new method is suggested in which the hull is represented by a doublet distribution rather than a source distribution. This approach which reduces computing time considerably permits improved accuracy and results in much better correlation between experimental and calculated values.

KEYWORDS

Propeller-induced Point Pressures

TABLE OF CONTENTS

Abstract	iii
Nomenclature	vii
INTRODUCTION	1
PROPELLER-INDUCED VIBRATORY PRESSURES AND FORCES ON A HULL	3
A. VELOCITY POTENTIAL	3
B. INTEGRAL EQUATION FOR THE HULL SOURCE DISTRIBUTION	4
C. PROPELLER-INDUCED VELOCITY FIELD	5
1) Due to Blade Loading	5
i) For the axial velocity component V_x	8
ii) For the radial velocity component V_r	9
iii) For the tangential velocity component V_ϕ	12
2) Due to Blade Thickness	13
i) For the axial velocity component V_{Tx}	15
ii) For the tangential velocity component, $V_{T\phi}$	16
iii) For the radial velocity component, V_{Tr}	16
D. SOLUTION OF THE INTEGRAL EQUATION	18
E. POINT PRESSURES ON THE HULL	19
1) Due to the Diffraction Potential	19
2) Free Space Pressure	21
i) Free space pressure due to propeller loading	21
ii) Pressure field due to propeller thickness	24
F. CORRELATIONS OF THEORY WITH EXPERIMENTS	25
G. CONCLUSIONS.	37
H. REFERENCES	39
APPENDIX	41
FIGURES (1-11)	

NOMENCLATURE

a	Ω/U
$c(\rho)$	expanded propeller chord at radius ρ
d	distance of propeller axis from free surface
$I_m(x)$	modified Bessel function of first kind of order m
$K_m(x)$	modified Bessel function of second kind
$\bar{K}(m, \bar{n})$	modified space function (after chordwise integration)
k	variable of integration
$L^{(\lambda, \bar{n})}(\rho) = L_{\lambda, \bar{n}}(\rho)$	spanwise blade loading, lb/ft
$\ell_{\lambda, \bar{n}}$	loading coefficients
ℓ	integer multiple
m	integer
N	number of blades
n	rps
\bar{n}	order of chordwise modes
P	pressure, lb/ft ²
q	order of harmonic of velocity field
R	Descartes distance
r_o	propeller radius, ft
S	surface
t	time, sec
U	free-stream velocity
u_x	axial component of velocity (hull axes system)
u	variable of integration
$V_{x, r, \varphi}$	axial, radial and tangential components of velocity field of propeller

$V_{x,y,z}$	velocity components in Cartesian coordinate system
w_z	vertical component of velocity (hull axes system)
X,Y,Z	hull Cartesian coordinate system
x,y,z	propeller Cartesian coordinates of field point
x,r,φ	propeller cylindrical coordinates of field point
$\Theta = -\Omega t$	= blade angular position
θ_b	projected propeller semichord, radians
$\Lambda^{(\bar{n})}(x)$	defined in Appendix
λ	order of harmonic of loading
λ	variable of integration
ξ,ρ,θ_0	cylindrical coordinates of point on propeller blade
ξ,η,ζ	hull Cartesian coordinates
ρ_f	mass density of fluid, slugs/cu ft
σ	source strength
σ'	angular measure of skewness
$\tau_0(\rho)$	maximum thickness of blade
Φ,φ	velocity potential
Ω	angular velocity of propeller

INTRODUCTION

Propeller-induced ship hull vibration continues to be a major uncertainty to the naval architect designing any class of ship. In all cases, the amelioration of hull vibration is desired, with different levels of tolerance since vibration causes discomfort to passengers and crew, produces material strain and fatigue and generates noise which impedes communications. With today's trend towards higher speed and larger ship dimensions, requiring greater power to be delivered to the propeller, the problem of propeller-induced hull vibration has become of paramount importance, necessitating improvement of the methods for predicting propeller-excited forces and moments. The methods have to be reliable and practical for use at the design stage. It is believed that only upon the development and use of a readily applicable set of computer programs can future vessels be designed which have reduced propeller-generated vibration.

Investigations^{(1,2)*} have been initiated to provide a satisfactory procedure and furnish adequate information to allow the naval architect to determine propeller-induced hull excitation. A generalization of the earlier procedures for prediction of propeller-generated vibratory hull forces on arbitrary hulls has recently been published.⁽³⁾ The task remaining is to demonstrate the reliability of this method by comparison of calculated pressures with E. Huse's⁽⁴⁾ extensive measurements of point pressures on a tanker model with $C_B = 0.80$.

The method of calculating the blade-frequency point pressure on the hull and the corresponding hydrodynamic forces and moments requires assuming a source distribution over the hull surface to simulate the ship in both uniform axial and propeller-generated flows. The strengths of the singularities are determined through the solution of a Fredholm integral equation of the second kind knowing the propeller-induced velocity on the hull. To carry out the numerical solution of the integral equation, the hull surface is subdivided into quadrilaterals. The quadrilateral size is crucial in calculating the hydrodynamic forces and point pressures, and the large number of quadrilaterals required to maintain the desired accuracy together with the complication arising from the calculations of the propeller-induced velocity, makes this numerical

*Superior numbers in text matter refer to similarly numbered references listed at the end of this report.

approach expensive and hence not attractive for practical application.

As mentioned in Reference 3, a new approach has been developed with MARAD support, in which the hull is represented by a distribution of doublets whose strength will be determined by the same integral equation as before, but with the known function replaced by the negative of the propeller velocity potential function. The latter has no directivity and, hence, there is only a single value at each point on the hull, whereas the present method requires calculation of three components of the propeller-induced velocity field to determine the normal velocity at each point on the hull surface. The computer time for evaluating the strength of the doublet distribution is considerably less than that currently required for the determination of the hull-source-density distribution and as has been seen, greater accuracy can be achieved within a shorter time. This will be further demonstrated in a future study correlating predicted and experimental values for forces on the Series 60 hull and point pressures on Huse's tanker model.⁽⁴⁾

The present study is sponsored by the Naval Sea Systems Command, General Hydromechanics Research Program, under Contract N00014-79-C-0240, administered by the David W. Taylor Naval Ship Research and Development Center.

PROPELLER-INDUCED VIBRATORY PRESSURES AND FORCES ON A HULL

A. VELOCITY POTENTIAL

Let the velocity potential of a ship stationary in uniform flow of velocity U along the $+X$ direction (see Figure 1) in the presence of an operating propeller, with and without free surface, be denoted by φ_s . When the propeller-induced pressure and velocity fields are calculated, the fact that the propeller operates in a spatially varying inflow field must be taken into account. The presence or absence of the free surface should be taken into account by a proper image system reflecting the fact that the free surface behaves either like a "rigid wall" or a surface of constant pressure.

The ship velocity potential can be expressed as

$$\varphi_s = \varphi_{ss} + \varphi_{sp} \quad (1)$$

where φ_{ss} is the velocity potential of a ship in a uniform stream ($+U$) and φ_{sp} the potential of the ship in the presence of the propeller-induced velocity field.

When the ship hull is represented by a source distribution over the hull surface, the first potential will be given as

$$\varphi_{ss} = - \frac{1}{4\pi} \int_S \sigma_o \left(\frac{1}{R} + \frac{1}{R_i} \right) dS \quad (2)$$

where σ_o is the source density which creates the hull in the presence of a uniform stream U ; R and R_i are the Descartes distances to any field point $P(X,Y,Z)$ from any hull point $Q(\xi,\eta,\zeta)$ and its corresponding positive image in the free surface; S is the wetted hull surface. Taking into account the symmetry of the flow with respect to the waterplane, and the symmetry of the hull with respect to the centerplane, the image system is constructed so that the "zero" Froude number or "rigid wall" condition is satisfied under the assumption that the ship speed is low.

When the ship hull is represented by a source distribution of density σ over the wetted hull surface to create the hull in the presence of the propeller and its negative image in the waterplane, then the ship velocity

potential is given as

$$\varphi_{sp} = -\frac{1}{4\pi} \int_S \sigma \left(\frac{1}{R} - \frac{1}{R_i} \right) dS \quad (3)$$

where R and R_i are the Descartes distances to a field point P from a hull point Q and its image point Q_i ; σ is the blade-frequency dependent source density.

It is clear that for all points on the free surface where $R=R_i$ the high Froude number limiting condition $\varphi_{sp} = 0$ is satisfied.

B. INTEGRAL EQUATION FOR THE HULL SOURCE DISTRIBUTION

It is assumed that the ship hull is represented by a distribution of sources over the hull surface of unknown density σ , which is determined by the requirement that their normal velocity balance any incident flow. This required kinematic boundary condition yields the following integral equation for the unknown source density distribution, $\sigma(P)$,

$$2\pi\sigma(P) - \int_S \sigma(Q) \frac{\partial}{\partial n} \frac{1}{R(P,Q)} dS = -v_n(P) \quad (4)$$

where $\frac{1}{R}$ represents either the kernel of Eq.(2) or Eq.(3). In either case, $\frac{\partial}{\partial n}$ is the derivative normal to the hull surface at point P ; S is the wetted surface of the hull. This equation is a Fredholm integral equation of the second kind for the unknown source densities σ , which are determined in terms of the known onset flow on the hull surface specified on the right-hand side of the equation. The following flow field imposed on the locus of the hull is considered: a flow imposed on the hull due to uniform longitudinal flow and two components, the real and imaginary parts of the blade frequency velocity field induced by the action of the propeller. For each given onset flow, the source densities are computed by solving Eq.(4).

The coded numerical procedure developed by Hess-Smith⁽⁵⁾ is applied to solve this integral equation. The three onset flows considered produce three densities, namely, σ_o , due to the uniform steady flow and σ_R and σ_I due to the real and imaginary parts of the onset flow due to the propeller and its image in the free surface corresponding to high frequency Froude number. The use of the negative image of the propeller located at the reflected position above the free surface satisfies the high Froude number

conditions on the free surface. For points on the free surface, this condition yields zero perturbation pressure or equivalently doubles the vertical component of the velocity induced by the direct propeller.

Thus the inversion of the integral equation is achieved by a numerical procedure implemented by the Hess-Smith program,⁽⁵⁾ provided the right-hand side is known. This part constitutes the major computing effort of this endeavor.

C. PROPELLER-INDUCED VELOCITY FIELD

1) Due to Blade Loading

Considerable effort has been devoted to the development of an unsteady lifting surface theory for propellers operating in a spatially nonuniform hull wake. The theoretical analysis and numerical techniques developed at Davidson Laboratory are based on modeling the propeller blades with sources and pressure dipole singularities. The computer program permits the calculation of steady and unsteady blade pressure distributions and resulting bearing forces and moments for a given propeller geometry (i.e., number of blades, pitch, chord length, camber, thickness, skew) and a given inflow field. Details of the theory, numerical analysis, and computer programs have been reported elsewhere.^(6,7) The theory has been extended to compute the field point velocities^(8,9) and pressures.^(10,11)

The steady and unsteady blade loadings are used to calculate their field point inductions as responses to the propeller blades operating in the hull wake. The wake survey has been harmonically analyzed in terms of the shaft rotation frequency, and, upon summing over all the blades, only certain harmonics contribute to the net exciting forces and moments acting on the shaft, namely, ℓN for the thrust and torque and $\ell N \pm 1$ for the side-bearing forces and moments where ℓ is any integer and N is the number of blades. However, all the harmonics of loading contribute to the forces on an individual blade and to the blade rate of radiated velocity and radiated pressure fields of the propeller (e.g., at points on the hull surface).

The velocity potential at a point (x, r, φ) (in the propeller coordinate system)* due to the loading of an N -bladed propeller operating in a spatially

*See Figures 2, 3 and 4.

varying inflow field is given^(8,9) by,

$$\Phi(x, r, \varphi; q) = \operatorname{Re} \int_{\rho} \sum_{\bar{n}=1}^{\infty} \sum_{\lambda=0}^{\infty} L(\lambda, \bar{n})(\rho) e^{iq\Omega t} \bar{K}(m, \bar{n}) d\rho$$

where the function $\bar{K}(m, \bar{n})$, which is known as the propagation or influence function, is given for $q=\ell N$, $m=\lambda-\ell N$, by

$$\begin{aligned} \bar{K}(m, \bar{n}) = & - \frac{i N e^{im(\sigma' - \varphi)}}{4\pi \rho_f U a} \left\{ e^{i\ell N(\sigma' - ax)} \left(\frac{m}{\rho^2} - a^2 \ell N \right) \right. \\ & \cdot I_m(a|\ell N|\rho) K_m(a|\ell N|r) \Lambda^{(\bar{n})}(\lambda \theta_b) - \frac{i}{\pi} \int_{-\infty}^{\infty} e^{ik(x - \sigma'/a)} \\ & \cdot \left. \frac{(m/\rho^2 + ak)}{k + a\ell N} I_m(|k|\rho) K_m(|k|r) \cdot \Lambda^{(\bar{n})} \left[\left(m - \frac{k}{a} \right) \theta_b \right] dk \right\} \quad (5) \end{aligned}$$

for $\rho < r$ (for $\rho > r$, ρ and r are interchanged in the modified Bessel functions). The symbol $\Lambda^{(\bar{n})}(x)$ denotes the results of the chordwise integration which differs with the assumed chordwise modes (see Appendix).

The velocities in the x , y , and z directions of the Cartesian coordinate system with origin at the propeller center at a point x, r, φ due to the propeller operating in spatially varying inflow will be given by the appropriate components of the gradient of the velocity potential Φ .

The axial component in nondimensional form is

$$\frac{V_x}{U} = \frac{\Phi_x}{U} \quad (6)$$

and the y and z components are derived from

$$\begin{aligned} \frac{V_y}{U} = \frac{\Phi_y}{U} &= - \frac{\Phi_r}{U} \sin \varphi - \frac{1}{r} \frac{\Phi_\varphi}{U} \cos \varphi \\ \frac{V_z}{U} = \frac{\Phi_z}{U} &= \frac{\Phi_r}{U} \cos \varphi - \frac{1}{r} \frac{\Phi_\varphi}{U} \sin \varphi \end{aligned} \quad (7)$$

where Φ_r and Φ_φ are given by the derivatives with respect to r and φ of the velocity potential (Eq.5).

In nondimensional form in the steady state, nonuniform inflow case,
 $q=\ell=0$, $m=\lambda$

$$\begin{aligned}\frac{v_x^{(0)}}{U} &= \frac{\Phi_x^{(0)}}{U} = \int_{\rho} \sum_{\bar{n}=1} \sum_{\lambda=0} L^{(\lambda, \bar{n})}(\rho) \bar{K}_x^{(\lambda, \bar{n})} d\rho \\ \frac{v_r^{(0)}}{U} &= \frac{\Phi_r^{(0)}}{U} = \int_{\rho} \sum_{\bar{n}=1} \sum_{\lambda=0} L^{(\lambda, \bar{n})}(\rho) \bar{K}_r^{(\lambda, \bar{n})} d\rho \\ \frac{v_{\varphi}^{(0)}}{U} &= \frac{\Phi_{\varphi}^{(0)}}{r r_o U} = \frac{1}{r} \int_{\rho} \sum_{\bar{n}=1} \sum_{\lambda=0} L^{(\lambda, \bar{n})}(\rho) \bar{K}_{\varphi}^{(\lambda, \bar{n})} d\rho\end{aligned}\quad (8)$$

and in the unsteady blade frequency case, $q=N$, $|\ell|=1$ and $m=\lambda-N$

$$\begin{aligned}\frac{v_x^{(N)}}{U} &= \frac{\Phi_x^{(N)}}{U} = \int_{\rho} \sum_{\bar{n}=1} \sum_{\lambda=0} \left\{ L^{(\lambda, \bar{n})}(\rho) \bar{K}_x^{(\lambda-N, \bar{n})} \right. \\ &\quad \left. + \text{conj.} \left[L^{(\lambda, \bar{n})}(\rho) \bar{K}_x^{(\lambda+N, \bar{n})} \right] \right\} d\rho \\ \frac{v_r^{(N)}}{U} &= \frac{\Phi_r^{(N)}}{U} = \int_{\rho} \sum_{\bar{n}=1} \sum_{\lambda=0} \left\{ L^{(\lambda, \bar{n})}(\rho) \bar{K}_r^{(\lambda-N, \bar{n})} \right. \\ &\quad \left. + \text{conj.} \left[L^{(\lambda, \bar{n})}(\rho) \bar{K}_r^{(\lambda+N, \bar{n})} \right] \right\} d\rho \\ \frac{v_{\varphi}^{(N)}}{U} &= \frac{\Phi_{\varphi}^{(N)}}{r r_o U} = \frac{1}{r} \int_{\rho} \sum_{\bar{n}=1} \sum_{\lambda=0} \left\{ L^{(\lambda, \bar{n})}(\rho) \bar{K}_{\varphi}^{(\lambda-N, \bar{n})} \right. \\ &\quad \left. + \text{conj.} \left[L^{(\lambda, \bar{n})}(\rho) \bar{K}_{\varphi}^{(\lambda+N, \bar{n})} \right] \right\} d\rho\end{aligned}\quad (9)$$

where it is seen that the propeller induced velocity field is made up of a large number of combinations of the frequency constituents of the loading function with those of the so-called "propagation function" $\bar{K}^{(m, \bar{n})}$. In uniform inflow the only blade loadings present are at $\lambda=0$. The corresponding velocities are obtained by restricting Eqs. (8) and (9) to the $\lambda=0$ terms.

The program requires that the field points be in cylindrical coordinates x, r, φ with origin at the propeller center. The axial x positive aft, and radial r distances are in terms of propeller radius. The angular ordinate φ is measured counterclockwise from the vertical (12M) position looking forward for the direct system. The connections between cylindrical and rectangular propeller coordinates, with y positive to starboard and z positive upward are for the direct system: $r = \sqrt{y^2 + z^2}$, $\varphi = \tan^{-1}(-y/z)$, $-\pi \leq \varphi \leq \pi$. For the image propeller, $r_i = \sqrt{y^2 + (2d-z)^2}$, $\varphi_i = \tan^{-1}(-y/(2d-z))$ measured clockwise from the 6 o'clock position, where d = distance of the propeller axis from the free surface. For the image propeller the formula for V_z/U in Eq.(7) is opposite in sign.

The propagation functions were given first in References 8 and 9. They were given later in Reference 11, the documentation of the computer program for the propeller-generated velocity field, with some changes in sign to agree with the sign convention of Reference 10 for the pressure field. They are repeated here with the correct signs⁽¹¹⁾ to obviate confusion.

i) For the axial velocity component V_x

$$\begin{aligned} \bar{K}_x(m, \bar{n}) = & + \frac{Ne^{i(\lambda\sigma' - m\varphi - a\ell N x)}}{4\pi\rho_f U^2 a r_o} \\ & \cdot \left\{ a\ell N(a^2\ell N - m/\rho^2) I_m(a|\ell N|\rho) K_m(a|\ell N|r) \Lambda^{(\bar{n})}(\lambda\theta_b) \right. \\ & \left. - \frac{i}{\pi} \int_0^\infty \frac{h(u) - h(-u)}{u} du \right\} \quad \text{for } \rho \leq r \end{aligned} \quad (10)$$

where $h(u) = (u - a\ell N)(au - a^2\ell N + m/\rho^2) I_m(|u - a\ell N|\rho)$

$$\cdot K_m(|u - a\ell N|r) e^{iu(x - \sigma'/a)} \Lambda^{(\bar{n})}[(\lambda - u/a)\theta_b]$$

The integrand at $u=0$ is evaluated in Reference 8 as

(a) When $q=\ell=0$, $m=\lambda=0$

$$\lim_{u \rightarrow 0} \left[\frac{h(u) - h(-u)}{u} \right] = 0$$

(b) When $q=l=0$, $m=\lambda \neq 0$

$$\lim_{u \rightarrow 0} \left[\frac{h(u) - h(-u)}{u} \right] = \begin{cases} (1/\rho^2) (\rho/r)^m \Lambda^{(\bar{n})}(\lambda \theta_b) & \text{for } \rho \leq r \\ (1/\rho^2) (r/\rho)^m \Lambda^{(\bar{n})}(\lambda \theta_b) & \text{for } \rho \geq r \end{cases}$$

(c) When $q=lN \neq 0$

$$\begin{aligned} \lim_{u \rightarrow 0} \left[\frac{h(u) - h(-u)}{u} \right] = & -2 \{ I_m(a|lN|\rho) K_m(a|lN|r) \} \\ & \cdot \{ [2a^2 lN - m/\rho^2 - i(x - \sigma'/a) a lN (a^2 lN - m/\rho^2)] \Lambda^{(\bar{n})}(\lambda \theta_b) \\ & - i \theta_b lN (a^2 lN - m/\rho^2) \Lambda_1^{(\bar{n})}(\lambda \theta_b) \} \\ & \mp \{ \rho K_m(a|lN|r) [I_{m-1}(a|lN|\rho) + I_{m+1}(a|lN|\rho)] - r I_m(a|lN|\rho) \\ & \cdot [K_{m-1}(a|lN|r) + K_{m+1}(a|lN|r)] \} \cdot a lN (a^2 lN - m/\rho^2) \Lambda^{(\bar{n})}(\lambda \theta_b), \text{ for } \rho \leq r \end{aligned}$$

where the upper sign (-) is used when $l > 0$ and the lower sign (+) when $l < 0$. When $\rho > r$, ρ and r are interchanged in the factors in braces (involving modified Bessel functions and their derivatives). For $\Lambda_1^{(\bar{n})}(x)$, see Appendix.

The closed term of (10) can be shown to be equal to zero when $q=l=0$.

ii) For the radial velocity component V_r

When $\rho < r$

$$\begin{aligned} \bar{K}_r^{(m, \bar{n})}(\rho < r) = & \frac{+Ne^{i(\lambda \sigma' - m\varphi - a lN x)}}{4\pi \rho_f U^2 a r_0} \\ & \cdot \left\{ -\frac{i}{2} a lN (a^2 lN - m/\rho^2) I_m(a|lN|\rho) [K_{m-1}(a|lN|r) \right. \\ & \left. + K_{m+1}(a|lN|r) \Lambda^{(\bar{n})}(\lambda \theta_b) + \frac{1}{2\pi} \int_0^\infty \frac{g_1(u) - g_1(-u)}{u} du \right\} \end{aligned} \quad (11a)$$

$$\text{where } g_1(u) = |u - a\ell N| (au - a^2 \ell N + m/\rho^2) I_m(|u - a\ell N| \rho) \\
\cdot [K_{m-1}(|u - a\ell N| r) + K_{m+1}(|u - a\ell N| r)] \\
\cdot e^{iu(x - \sigma'/a)} \Lambda^{(\bar{n})}[(\lambda - u/a)\theta_b] .$$

It can easily be shown that when $q=\ell=0$ the closed term of (11a) becomes

$$(i/2)(\rho/r)^m (m/r\rho^2) \Lambda^{(\bar{n})}(\lambda\theta_b)$$

where $m=\lambda$ since $q=0$.

The integrand at $u=0$ is evaluated⁽⁸⁾ as

(a) When $q=\ell=0$, $m=\lambda=0$

$$\lim_{u \rightarrow 0} \left[\frac{g_1(u) - g_1(-u)}{u} \right] = (4a/r) \Lambda^{(\bar{n})}(0)$$

(b) When $q=\ell=0$, $m=\lambda \neq 0$

$$\lim_{u \rightarrow 0} \left[\frac{g_1(u) - g_1(-u)}{u} \right] = (2/r)(\rho/r)^m \\
\cdot \{ [a + (im/\rho^2)(x - \sigma'/a)] \Lambda^{(\bar{n})}(\lambda\theta_b) + (im/\rho^2)(\theta_b/a) \Lambda_1^{(\bar{n})}(\lambda\theta_b) \}$$

(c) When $q=\ell N \neq 0$

$$\lim_{u \rightarrow 0} \left[\frac{g_1(u) - g_1(-u)}{u} \right] = \pm 2 \{ I_m(a|\ell N| \rho) [K_{m-1}(a|\ell N| r) \\
+ K_{m+1}(a|\ell N| r)] \} \{ [2a^2 \ell N - m/\rho^2 - i(x - \sigma'/a)(a\ell N)(a^2 \ell N - m/\rho^2)] \Lambda^{(\bar{n})}(\lambda\theta_b) \\
- i\theta_b \ell N (a^2 \ell N - m/\rho^2) \Lambda_1^{(\bar{n})}(\lambda\theta_b) \} + a\ell N (a^2 \ell N - m/\rho^2) \Lambda^{(\bar{n})}(\lambda\theta_b) \\
\cdot \{ \rho [I_{m-1}(a|\ell N| \rho) + I_{m+1}(a|\ell N| \rho)] [K_{m-1}(a|\ell N| r) + K_{m+1}(a|\ell N| r)] \\
- r I_m(a|\ell N| \rho) [K_{m-2}(a|\ell N| r) + 2K_m(a|\ell N| r) + K_{m+2}(a|\ell N| r)] \}$$

where the upper sign (+) is used when $\ell > 0$ and the lower sign (-) when $\ell < 0$.

When $\rho > r$

$$\begin{aligned} \bar{K}_r^{(m, \bar{n})}(\rho > r) = & + \frac{N e^{i(\lambda \sigma' - m \varphi - a \ell N x)}}{4 \pi \rho_f U^2 a r_o} \cdot \left\{ + (i/2) a \ell N I(a^2 \ell N - m/\rho^2) K_m(a \ell N | \rho) \right. \\ & \cdot [I_{m-1}(a \ell N | r) + I_{m+1}(a \ell N | r)] \Lambda^{(\bar{n})}(\lambda \theta_b) \\ & \left. + (1/2\pi) \int_{-\infty}^{\infty} \frac{g_2(u) - g_2(-u)}{u} du \right\} \end{aligned} \quad (11b)$$

where $g_2(u) = -[u - a \ell N I(a u - a^2 \ell N + m/\rho^2) K_m(u - a \ell N | \rho)]$

$$\cdot [I_{m-1}(u - a \ell N | r) + I_{m+1}(u - a \ell N | r)] \cdot e^{i u (x - \sigma'/a)} \Lambda^{(\bar{n})}[(\lambda - u/a) \theta_b]$$

In this case when $q = \ell = 0$, the closed term is

$$-(i/2) (r/\rho)^m (m/r \rho^2) \Lambda^{(\bar{n})}(\lambda \theta_b)$$

The integrand at $u=0$ is evaluated⁽⁸⁾ as

(a) When $q = \ell = 0$, $m = \lambda = 0$

$$\lim_{u \rightarrow 0} \left[\frac{g_2(u) - g_2(-u)}{u} \right] = 0$$

(b) When $q = \ell = 0$, $m = \lambda \neq 0$

$$\lim_{u \rightarrow 0} \left[\frac{g_2(u) - g_2(-u)}{u} \right] = (-2/r) (r/\rho)^m$$

$$\cdot \{ [a + (im/\rho^2)(x - \sigma'/a)] \Lambda^{(\bar{n})}(\lambda \theta_b) + (im/\rho^2)(\theta_b/a) \Lambda_1^{(\bar{n})}(\lambda \theta_b) \}$$

(c) When $q = \ell N \neq 0$

$$\begin{aligned} \lim_{u \rightarrow 0} \left[\frac{g_2(u) - g_2(-u)}{u} \right] &= \mp 2K_m(a|\ell N|\rho) [I_{m-1}(a|\ell N|r) + I_{m+1}(a|\ell N|r)] \\ &\cdot \{ [2a^2 \ell N - m/\rho^2 - i(x - \sigma'/a)a \ell N(a^2 \ell N - m/\rho^2)] \Lambda^{(\bar{n})}(\lambda \theta_b) \\ &- i\theta_b \ell N(a^2 \ell N - m/\rho^2) \Lambda_1^{(\bar{n})}(\lambda \theta_b) \} + (a \ell N)(a^2 \ell N - m/\rho^2) \Lambda^{(\bar{n})}(\lambda \theta_b) \\ &\cdot \{ \rho [K_{m-1}(a|\ell N|\rho) + K_{m+1}(a|\ell N|\rho)] [I_{m-1}(a|\ell N|r) + I_{m+1}(a|\ell N|r)] \\ &- r K_m(a|\ell N|\rho) [I_{m-2}(a|\ell N|r) + 2I_m(a|\ell N|r) + I_{m+2}(a|\ell N|r)] \} \end{aligned}$$

where the upper sign (-) is used when $\ell > 0$ and the lower sign (+) when $\ell < 0$.

When $\rho = r$, then

$$\bar{K}_r^{(m, \bar{n})}(\rho=r) = [\text{Eq. (11a)} + \text{Eq. (11b)}] \text{ evaluated at } \rho=r. \quad (11c)$$

iii) For the tangential velocity component V_φ

$$\begin{aligned} \bar{K}_\varphi^{(m, \bar{n})} &= + \frac{Ne^{i(\lambda \sigma' - m\varphi - a \ell N x)}}{4\pi \rho_f U^2 a r_o} \cdot \left\{ m(a^2 \ell N - m/\rho^2) I_m(a|\ell N|\rho) K_m(a|\ell N|r) \Lambda^{(\bar{n})}(\lambda \theta_b) \right. \\ &\quad \left. + (i/\pi) \int_0^\infty m \left[\frac{f(u) - f(-u)}{u} \right] du \right\} \quad (12) \end{aligned}$$

where

$$f(u) = (au - a^2 \ell N + m/\rho^2) I_m(|u - a \ell N|\rho) K_m(|u - a \ell N|r) \cdot e^{iu(x - \sigma'/a)} \Lambda^{(\bar{n})}[(\lambda - u/a)\theta_b]$$

It can be shown that when $q = \ell = 0$, the closed term of (12) becomes

$$(-m/2\rho^2)(\rho/r)^m \Lambda^{(\bar{n})}(\lambda \theta_b) \quad \text{for } \rho \leq r$$

$$(-m/2\rho^2)(r/\rho)^m \Lambda^{(\bar{n})}(\lambda \theta_b) \quad \text{for } \rho \geq r$$

The integrand of (12) evaluated for $u=0$ yields

(a) When $q = \ell = 0$, $m = \lambda = 0$

$$\lim_{u \rightarrow 0} m \left[\frac{f(u) - f(-u)}{u} \right] = 0$$

(b) When $q=\ell=0$, $m=\lambda \neq 0$

$$\lim_{u \rightarrow 0} m \left[\frac{f(u) - f(-u)}{u} \right] = \{ [a + i(x-\sigma^1/a)m/\rho^2] \Lambda^{(\bar{n})}(\lambda \theta_b) + (i\theta_b/a)(m/\rho^2) \Lambda_1^{(\bar{n})}(\lambda \theta_b) \} \begin{cases} (\rho/r)^m & \text{for } \rho \leq r \\ (r/\rho)^m & \text{for } \rho \geq r \end{cases}$$

(c) When $q=\ell N \neq 0$, $m=\lambda - \ell N$

$$\begin{aligned} \lim_{u \rightarrow 0} m \left[\frac{f(u) - f(-u)}{u} \right] = & +2m \{ [a + i(x-\sigma^1/a)(a^2 \ell N - m/\rho^2) \Lambda^{(\bar{n})}(\lambda \theta_b) - \\ & - (i\theta_b/a)(a^2 \ell N - m/\rho^2) \Lambda_1^{(\bar{n})}(\lambda \theta_b) \} I_m(a|\ell N|r) K_m(a|\ell N|r) \\ & \pm m(a^2 \ell N - m/\rho^2) \Lambda^{(\bar{n})}(\lambda \theta_b) \\ & \cdot \{ \rho K_m(a|\ell N|r) [I_{m-1}(a|\ell N|r) + I_{m+1}(a|\ell N|r)] \\ & - r I_m(a|\ell N|r) [K_{m-1}(a|\ell N|r) + K_{m+1}(a|\ell N|r)] \} \end{aligned}$$

for $\rho \leq r$, otherwise ρ and r are interchanged in the product of the modified Bessel functions and its derivative (the factor in braces in the second term). Here the upper sign (+) is used when $\ell > 0$ and the lower sign (-) when $\ell < 0$.

When $m=0$, i.e., $\lambda=\ell N$ whatever the value of ℓ ,

$$\bar{K}_\phi^{(m, \bar{n})} = 0.$$

2) Due to Blade Thickness

In considering the blade thickness, it must be remembered that the marine propeller with its blade describing a helicoidal surface is one of the few nonplanar lifting surfaces. The blade thickness plays a dual role, influencing both lifting and nonlifting characteristics of the blade. As part of the nonplanar surface, it induces a continuous component of velocity on points of the surface itself, thus affecting the blade loading distribution. The symmetrical flow disturbance caused by the blade thickness influences the pressure distributions on the suction and pressure sides of the blade without contributing to the net loading. The so-called "nonplanar

thickness" has been shown to have small effect on the blade loading and hydrodynamic forces and moments and presumably negligible effect on the velocity and pressure fields in the neighborhood of the operating propeller. The so-called "symmetrical flow disturbance" thickness has an appreciable effect on the blade pressure distribution and a sizable effect on the velocity field as well.

In this present study the effect of the "nonplanar" thickness has been neglected in evaluating the propeller loading, but the effect of the symmetrical blade thickness distribution is included by using the thin-body approximation. The blade cross-section is approximated as an intersecting of two circular arcs (i.e., lenticular cross-section) and it is represented by a source-sink distribution smeared over the blade area.⁽⁹⁾ This approximation was shown to be justifiable for calculating velocities at points in the field but not on the propeller.

The velocity potential due to the blade thickness is thus given as

$$\begin{aligned} \Phi_T(x, r, \varphi; t) = & \frac{-i2aNU}{\pi^2} \sum_{\ell=-\infty}^{\infty} e^{-i\ell N(\varphi + \Omega t)} e^{ia\ell N x} \int_{\rho} \frac{(1+a^2\rho^2)}{\theta_b} \frac{t_o(\rho)}{c(\rho)} \\ & \cdot \int_0^{\infty} \frac{[\sin(\lambda\theta_b/a) - (\lambda\theta_b/a)\cos(\lambda\theta_b/a)]}{\lambda^2} \\ & \cdot \{ I_{\ell N}(|\lambda + a\ell N|\rho) K_{\ell N}(|\lambda + a\ell N|r) e^{i\lambda(x-\sigma'/a)} \\ & - I_{\ell N}(|-\lambda + a\ell N|\rho) K_{\ell N}(|-\lambda + a\ell N|r) e^{-i\lambda(x-\sigma'/a)} \} d\lambda d\rho, \text{ for } \rho < r \end{aligned} \quad (13)$$

The velocity components along the x, y, and z coordinate axes will be given by Eqs. (6) and (7).

i) Axial velocity component, V_{TX}

Taking the derivative of Eq.(13) with respect to x

$$\begin{aligned} \frac{V_{TX}}{U} = \frac{\partial \Phi(x, r, \varphi; t)}{U \partial x} = & + \frac{2aN}{\pi^2} \sum_{\ell=-\infty}^{\infty} e^{-i\ell N \Omega t} e^{i\ell N(ax-\varphi)} \\ & \cdot \int_p \frac{(1 + a^2 \rho^2)}{\theta_b} \frac{t_o(\rho)}{c(\rho)} \int_0^{\infty} F(\lambda) [(\lambda + a\ell N)G(\lambda, \ell) \\ & + (\lambda - a\ell N)G(-\lambda, \ell)] d\lambda d\rho \end{aligned} \quad (14)$$

where

$$\begin{aligned} F(\lambda) &= [\sin(\lambda \theta_b / a) - (\lambda \theta_b / a) \cos(\lambda \theta_b / a)] / \lambda^2 \\ G(\lambda, \ell) &= I_{\ell N}(1\lambda + a\ell N | \rho) K_{\ell N}(1\lambda + a\ell N | r) e^{i\lambda(x-\sigma'/a)} \\ G(-\lambda, \ell) &= I_{\ell N}(1-\lambda + a\ell N | \rho) K_{\ell N}(1-\lambda + a\ell N | r) e^{-i\lambda(x-\sigma'/a)} \end{aligned} \quad (15)$$

It can be shown that the integrand is zero when $\lambda=0$. Equation (14) is written for $\rho < r$. For $\rho > r$, ρ and r are interchanged in the modified Bessel functions.

In the unsteady blade-frequency case, $|\ell| = 1$, the axial velocity is (cf Reference 8)

$$\begin{aligned} \frac{V_{TX}^{(-N)}}{U} + \text{conj.} \frac{V_{TX}^{(N)}}{U} &= \frac{2V_{TX}^{(-N)}}{U} \quad (\ell = -1) \\ &= + \frac{4aN}{\pi^2} e^{-iN(ax-\varphi)} \int_p \frac{(1 + a^2 \rho^2)}{\theta_b} \frac{t_o(\rho)}{c(\rho)} \\ &\quad \cdot \int_0^{\infty} F(\lambda) [(\lambda - aN)G(\lambda, -1) + (\lambda + aN)G(-\lambda, -1)] d\lambda d\rho \end{aligned} \quad (16)$$

In the steady state case, $\ell = 0$

$$\begin{aligned} \frac{V_{TX}^{(0)}}{U} &= + \frac{4aN}{\pi^2} \int_p \frac{(1 + a^2 \rho^2)}{\theta_b} \frac{t_o(\rho)}{c(\rho)} \\ &\quad \cdot \int_0^{\infty} \lambda F(\lambda) I_0(\lambda \rho) K_0(\lambda r) \cos[\lambda(x-\sigma'/a)] d\lambda d\rho \end{aligned} \quad (17)$$

ii) Tangential velocity component, $V_{\tau\varphi}$

The nondimensional tangential velocity is given by

$$\frac{V_{\tau\varphi}}{U} = - \frac{2aN}{r\pi^2} \sum_{\ell=-\infty}^{\infty} \ell N e^{-i\ell N[\Omega t - (ax - \varphi)]} \int_p \frac{(1 + a^2 \rho^2)}{\theta_b} \frac{t_o(\rho)}{c(\rho)} \cdot \int_0^{\infty} F(\lambda) [G(\lambda, \ell) - G(-\lambda, \ell)] d\lambda d\rho \quad (18)$$

The corresponding blade frequency component is given by

$$\frac{V_{\tau\varphi}^{(-N)}}{U} = + \frac{4aN^2}{r\pi^2} e^{-iN(ax - \varphi)} \int_p \frac{(1 + a^2 \rho^2)}{\theta_b} \frac{t_o(\rho)}{c(\rho)} \cdot \int_0^{\infty} F(\lambda) [G(\lambda, -1) - G(-\lambda, -1)] d\lambda d\rho \quad (19)$$

In the steady state case

$$\frac{V_{\tau\varphi}^{(0)}}{U} = 0 \quad (20)$$

iii) Radial velocity component, $V_{\tau r}$

The nondimensional blade frequency radial component will be given as

For $\rho < r$:

$$\begin{aligned} \frac{V_{\tau r}}{U} &= \frac{\partial \Phi_r(x, r, \varphi; t)}{U \partial r} = -i \frac{2aN}{\pi^2} \sum_{\ell=-\infty}^{\infty} e^{-i\ell N \Omega t} e^{i\ell N(ax - \varphi)} \\ &\quad \cdot \int_p \frac{(1 + a^2 \rho^2)}{\theta_b} \frac{t_o(\rho)}{c(\rho)} \int_0^{\infty} F(\lambda) \\ &\quad \cdot \left\{ I_{\ell N}(1 + a\ell N|\rho) \frac{\partial K_{\ell N}(1 + \lambda + a\ell N|r)}{\partial r} e^{i\lambda(x - \sigma'/a)} \right. \\ &\quad \cdot \left. - I_{\ell N}(1 - \lambda + a\ell N|\rho) \frac{\partial K_{\ell N}(1 - \lambda + a\ell N|r)}{\partial r} e^{-i\lambda(x - \sigma'/a)} \right\} d\lambda d\rho \end{aligned} \quad (21a)$$

For $\rho > r$:

$$\begin{aligned} \frac{V_{Tr}}{U} = & -i \frac{2aN}{\pi^2} \sum_{\ell=-\infty}^{\infty} e^{-i\ell N \Omega t} e^{i\ell N(ax-\varphi)} \int_{\rho} \frac{(1+a^2\rho^2)}{\theta_b} \frac{t_o(\rho)}{c(\rho)} \\ & \cdot \int_0^{\infty} F(\lambda) \left\{ K_{\ell N}(1+\ell N \rho) \frac{\partial I_{\ell N}(1+\ell N \rho)}{\partial r} e^{i\lambda(x-\sigma'/a)} \right. \\ & \left. - K_{\ell N}(1-\ell N \rho) \frac{\partial I_{\ell N}(1-\ell N \rho)}{\partial r} e^{-i\lambda(x-\sigma'/a)} \right\} d\lambda d\rho \end{aligned} \quad (21b)$$

For $\rho = r$:

$$\frac{V_{Tr}}{U} = [\text{Equation (21a)} + \text{Equation (21b)}] \text{ evaluated at } \rho = r \quad (21c)$$

Here

$$\frac{\partial K_{\ell N}(|c|r)}{\partial r} = -\frac{|c|}{2} [K_{\ell N-1}(|c|r) + K_{\ell N+1}(|c|r)]$$

and

$$\frac{\partial I_{\ell N}(|c|r)}{\partial r} = \frac{|c|}{2} [I_{\ell N-1}(|c|r) + I_{\ell N+1}(|c|r)]$$

In the steady state case, $\ell=0$:

$$\begin{aligned} \frac{V_{Tr}^{(0)}}{U} (\rho < r) = & -\frac{4aN}{\pi^2} \int_{\rho} \frac{(1+a^2\rho^2)}{\theta_b} \frac{t_o(\rho)}{c(\rho)} \\ & \cdot \int_0^{\infty} \lambda F(\lambda) I_0(\lambda\rho) K_1(\lambda r) \sin[\lambda(x-\sigma'/a)] d\lambda d\rho \end{aligned} \quad (22a)$$

$$\begin{aligned} \frac{V_{Tr}^{(0)}}{U} (\rho > r) = & +\frac{4aN}{\pi^2} \int_{\rho} \frac{(1+a^2\rho^2)}{\theta_b} \frac{t_o(\rho)}{c(\rho)} \\ & \cdot \int_0^{\infty} \lambda F(\lambda) K_0(\lambda\rho) I_1(\lambda r) \sin[\lambda(x-\sigma'/a)] d\lambda d\rho \end{aligned} \quad (22b)$$

$$\frac{V_{Tr}^{(0)}}{U} (\rho = r) = [\text{Equation (22a) + Equation (22b)}] \text{ evaluated at } \rho = r \quad (22c)$$

In the unsteady, blade-frequency case $|\ell|=1$, the radial component is obtained as

$$\frac{V_{Tr}^{(-N)}}{U} + \text{conj.} \frac{V_{Tr}^{(N)}}{U} = 2 \cdot \frac{V_{Tr}^{(-N)}}{U} (\ell = -1) \quad ; \quad (23)$$

that is, twice Eqs.(21a), (21b), or (21c) with $\ell = -1$.

A computer program has been developed and adapted to the CDC high-speed digital computer for the evaluation of the field point velocities,^(8,9,11) provided the propeller blade loadings have already been evaluated through another numerical code designated as PPEXACT.⁽⁷⁾ Thus, the necessary information for the solution of the integral Eq.(4) has been established.

D. SOLUTION OF THE INTEGRAL EQUATION

Equation (4) is inverted by using the Hess-Smith program developed at McDonnell-Douglas Aircraft Corporation. It should be noted, however, that the hull and its boundary conditions are referred to a new Cartesian coordinate system attached to the hull, as shown in Figure 1. The X-axis is in the same direction as x attached to the propeller, the Z-axis is towards starboard as is the y -axis in the propeller coordinate system, and the +Y-axis is vertically downwards opposite in direction to the z -axis of the propeller system with the XZ-plane taken to be the waterplane. The relation between the two coordinate systems is taken into consideration in the program. Only the hull coordinates of points on the hull surface are specified as input to the program. Whenever there is a need to make use of the corresponding propeller coordinates, those are determined automatically by the program.

The hull surface is subdivided into a large number of quadrilateral elements, each of which is considered to be a source panel of uniform density. The boundary conditions (i.e., the propeller-induced point velocity field) are specified at the null point in each of the source panels, thus generating as many linear algebraic equations as there are unknown sources.

The quadrilateral size is crucial in obtaining the solution of the Fredholm integral equation and then calculating the hydrodynamic forces and moments. The dimensions are dictated by the propeller-induced velocity which is of oscillatory character. The patch dimensions should be selected so as to fit at least four quadrilaterals into one cycle of spatial oscillation wherever such oscillations are present. This requirement, however, increases the already large number of quadrilaterals considerably and, hence, the number of field points at which the three velocity components are to be evaluated with all the required combinations of the frequencies of the loading and propagation functions.

A new study has been undertaken at Davidson Laboratory to replace the present method, which represents the hull by a source distribution and requires calculation of three velocity components at each field point (null point), by a procedure which represents the hull by a doublet distribution and requires the calculation of only one function, the propeller velocity potential. This method permits decreasing the mesh size of the quadrilaterals and increasing the number while still reducing computer time and is shown to be a considerable improvement.

E. POINT PRESSURES ON THE HULL

1) Due to the Diffraction Potential

Having obtained σ , the strength of the sources through Eq.(4), the diffraction potential φ_D (designated as φ_{sp} in Eq.(3)) can be calculated, and by means of the extended Lagally Theorem, the unsteady hull force can be determined (see Eq.(24), Ref.3). Most importantly, the pressure field due to the diffraction potential is given as

$$P_D(X,Y,Z;t) = -\rho_f \left(\frac{\partial \varphi_D}{\partial t} + U \frac{\partial \varphi_D}{\partial X} \right) \quad (24)$$

If it is assumed that φ_D has simple harmonic time dependence, in fact, considering the blade frequency component only,

$$\tilde{\varphi}_D = |\tilde{\varphi}_D| e^{iN\Omega t}$$

then the blade frequency pressure due to the diffraction potential is

$$\tilde{P}_D = -i\rho N\Omega |\tilde{\varphi}_D| - \rho U \tilde{u}_X^D \quad (25)$$

where \tilde{u}_X^D , the corresponding axial component of the velocity is determined

as a by-product of the process of inverting the integral Eq.(4) by the Hess-Smith numerical code. It is seen that the convective term of the blade frequency pressure due to the diffraction potential can easily be determined from the available information. The time-dependent term requires an explicit expression of $\tilde{\varphi}_D$.

No attempt has been made to develop a computer program for the evaluation of the diffraction potential φ_D because of limited funding. The diffraction potential could be determined through an integration of the vertical components of the velocity, \tilde{w}_Z^D , along a vertical line from a given point on the hull, where the pressure is to be calculated, to the waterplane (free surface) where the potential is zero because of the invocation of the high frequency Froude number condition.

Through this vertical integration

$$\int_{\zeta_H}^{\zeta_S} \tilde{w}_Z^D(X,Y,Z) dZ = \int_{\zeta_H}^{\zeta_S} \frac{\partial \tilde{\varphi}_D}{\partial Z} dZ = \tilde{\varphi}_D(\zeta_S) - \tilde{\varphi}_D(\zeta_H) = - \tilde{\varphi}_D(\zeta_H)$$

since $\tilde{\varphi}_D(\zeta_S) = 0$ on the waterplane. Thus, the diffraction potential $\tilde{\varphi}$ is given by

$$\tilde{\varphi}_D = - \int_{\zeta_H}^{\zeta_S} \tilde{w}_Z^D(X,Y,Z) dZ \quad . \quad (26)$$

The vertical diffraction velocities required in this integration are given by successive application of the Hess-Smith program for off-body points,⁽⁵⁾ which may be particularized for points located inside the body. Care should be taken for points close to the surface of the body where there exists a sharp gradient of the velocity. Another difficulty is the fact that the smooth body is approximated by planar quadrilaterals so that the exact location of the body surface is no longer precisely known. To overcome this difficulty, a fine mesh size should be used. By plotting the results of the calculated velocities, the null points on the approximated body will clearly be indicated by the presence of a sharp discontinuity in velocity at the points across the boundary. Thus, the ordinates of the null points and the range of integration will be established.

All quantities have been computed in non-dimensional form, using the

model speed U and propeller radius r_o (for non-dimensionalizing the linear dimensions). The non-dimensional diffraction velocity potential (Eq.26) is given by

$$\tilde{\varphi}_D = -Ur_o \int_{\zeta_H'}^{\zeta_S'} \tilde{w}_Z'^D dz \quad (27)$$

and the corresponding expression for the blade frequency pressure (Eq.25) is given by

$$\tilde{p}_D^{(N)} = +i\rho N 2\pi n r_o \int_{\zeta_H'}^{\zeta_S'} \tilde{w}_Z' dz' - \rho U^2 \tilde{u}_X^D \quad (28)$$

with the substitution $\Omega = 2\pi n$, $n = \text{rps}$.

2) Free Space Pressure

These results must then be combined with pressures emanating from the propeller in the absence of the hull surface. These pressures are calculated utilizing the pressure field program⁽¹⁰⁾ in conjunction with the blade pressure program of Reference 7. For completeness of the present study, the expressions for these pressures are given below:

i) Free space pressure due to propeller loading

$$P(x, r, \varphi; t) = \int_{\rho} \sum_{\lambda=0}^{\infty} \sum_{\bar{n}=1}^{\bar{n}_{\max}} L_{\lambda, \bar{n}}(\rho) e^{i\lambda\Omega t} \sum_{m=-\infty}^{\infty} e^{-im\Omega t} K_{m, \bar{n}}(x, r, \varphi; \rho) \quad (29)$$

where, with ρ, r, x, k and a non-dimensionalized with respect to propeller radius r_o , the influence or spatial propagation function is

$$\begin{aligned} K_{m, \bar{n}}(x, r, \varphi; \rho) = & + \frac{Ni}{4\pi^2 a r_o} e^{im(\sigma' - \varphi)} \\ & \cdot \left\{ a \int_0^{\infty} k I_m(k\rho) K_m(kr) \left[e^{ik(x - \sigma'/a)_{\Lambda}(\bar{n})} \left((m - \frac{k}{a}) \theta_b \right) - e^{-ik(x - \sigma'/a)_{\Lambda}(\bar{n})} \left((m + \frac{k}{a}) \theta_b \right) \right] dk \right. \\ & \left. + \frac{m}{\rho^2} \int_0^{\infty} I_m(k\rho) K_m(kr) \left[e^{ik(x - \sigma'/a)_{\Lambda}(\bar{n})} \left((m - \frac{k}{a}) \theta_b \right) + e^{-ik(x - \sigma'/a)_{\Lambda}(\bar{n})} \left((m + \frac{k}{a}) \theta_b \right) \right] dk \right\} \quad (30) \end{aligned}$$

where for $m \neq 0$ and $k=0$, the integrand is equal to

$$\frac{1}{\rho^2} \frac{m}{|m|} \left(\frac{\rho}{r}\right)^{|m|} \Lambda^{(\bar{n})}(m\theta_b) \quad \text{for } \rho < r$$

and

$$\frac{1}{\rho^2} \frac{m}{|m|} \left(\frac{r}{\rho}\right)^{|m|} \Lambda^{(\bar{n})}(m\theta_b) \quad \text{for } r < \rho$$

When $m=0$, Eq.(30) becomes

$$K_{0,\bar{n}}(x,r,\varphi;\rho) = + \frac{Ni}{4\pi^2 a r_0} \left\{ 2ai \int_0^\infty k I_0(k\rho) K_0(kr) \right. \\ \left. \cdot \text{Imag. Part} \left[e^{ik(x-\sigma'/a)} \Lambda^{(\bar{n})} \left(-\frac{k}{a} \theta_b \right) \right] \right\} \quad (31)$$

In this case when $k=0$, the integrand is zero.

In computing the k -integral of (30) or (31) numerically, it must be realized that the integration interval Δk depends mainly on the range of x . The product of the modified Bessel functions decreases monotonically with increasing k , and the Λ function, although oscillatory, is damped out with increasing k . However, $\exp(\pm ikx)$ is undamped oscillatory and care must be taken to have sufficient ordinates in a cycle.

Using the following designation for simplicity

$$\ell_{\lambda,\bar{n}} k_{m,\bar{n}} = \sum_{i=1}^8 L_{\lambda,\bar{n}}(\rho_i) \int_{\rho_i-\beta}^{\rho_i+\beta} K_{m,\bar{n}}(x,r,\varphi;\rho) d\rho$$

where 2β is the spanwise strip length, then the pressure can be expressed as

$$P(x,r,\varphi;t) = \sum_{\bar{n}=1}^{\bar{n} \max} \sum_{\lambda=0}^{\infty} \sum_{m=-\infty}^{\infty} \ell_{\lambda,\bar{n}} k_{m,\bar{n}} e^{i(\lambda-m)\Omega t} \quad (32)$$

where only those terms must be summed for which $\lambda-m=\ell N$ and $\lambda-m=-\ell N$, $\ell = 0, 1, 2, \dots$

In the steady-state case (mean value) when $\ell=0$, then

$$P_0(x,r,\varphi) = \sum_{\bar{n}=1}^{\bar{n} \max} \sum_{\lambda=0}^{\infty} \ell_{\lambda,\bar{n}} k_{\lambda,\bar{n}} \quad (33)$$

In the unsteady case ($\ell > 0$) the pressure given by Eq.(32) can be written as

$$\begin{aligned}
 P(x, r, \varphi; t) &= \text{R.P.} \sum_{\ell=0}^{\infty} \sum_{\bar{n}=1}^{\bar{n} \max} \sum_{\lambda=0}^{\infty} \left[\ell_{\lambda, \bar{n}} k_{\lambda-\ell N, \bar{n}} e^{-i \ell N \theta} + \ell_{\lambda, \bar{n}} k_{\lambda+\ell N, \bar{n}} e^{+i \ell N \theta} \right] \\
 &= \text{R.P.} \sum_{\ell=0}^{\infty} \sum_{\bar{n}=1}^{\bar{n} \max} \sum_{\lambda=0}^{\infty} \left\{ \ell_{\lambda, \bar{n}} k_{\lambda-\ell N, \bar{n}} + \text{conj.} \left[\ell_{\lambda, \bar{n}} k_{\lambda+\ell N, \bar{n}} \right] \right\} e^{-i \ell N \theta}
 \end{aligned} \quad (34)$$

where Ωt has been replaced by $-\theta$, the blade angular position (see Figure 3).

The complex amplitude of the ℓ th blade frequency harmonic pressure is

$$P_{\ell N} = \sum_{\bar{n}=1}^{\bar{n} \max} \sum_{\lambda=0}^{\infty} \left\{ \ell_{\lambda, \bar{n}} k_{\lambda-\ell N, \bar{n}} + \text{conj.} \left[\ell_{\lambda, \bar{n}} k_{\lambda+\ell N, \bar{n}} \right] \right\} \quad (35)$$

It may be observed that the pressure field component at frequency ℓN generated by an operating propeller in nonuniform inflow is made up of linear combinations of terms proportional to blade loadings at all significant wake harmonics λ propagated by spatial functions of harmonic orders $m = \lambda - \ell N$ and $m = \lambda + \ell N$.

It is interesting to note that the propeller-induced pressure field in the uniform inflow case is remarkably different from that in the non-uniform case. In the uniform case, only the zero harmonic of loading exists, i.e., $\lambda=0$, and hence the corresponding pressure field is given by

- 1) For the mean (mean value, $\ell=0$, therefore $m=0$)

$$P_0(x, r) = \sum_{\bar{n}=1}^{\bar{n} \max} \ell_{0, \bar{n}} k_{0, \bar{n}} \quad (36)$$

- 2) For the ℓN th harmonic

$$P_{\ell N}(x, r, \varphi) = 2 \sum_{\bar{n}=1}^{\bar{n} \max} \ell_{0, \bar{n}} k_{-\ell N, \bar{n}} \quad (37)$$

One should appreciate that these amplitudes are strong near the propeller, but decay extremely rapidly with distance from the propeller.

ii) Pressure field due to propeller thickness

The effect of finite blade thickness is to produce a symmetrical disturbance of the fluid on each side of the surface of symmetry through the blade sections. The thickness distribution of the blade section is approximated by a source-sink distribution smeared over the section with strength determined by the "thin body" approximation.

Reference 10 gives the pressure due to blade thickness at multiples of blade frequency as

$$(P_T)_{\ell N}(\ell < 0) = -\rho_f U^2 \left\{ \frac{4a_N}{\pi^2} e^{i\ell N(ax-\varphi)} \int_{\rho} \frac{(1+a^2\rho^2)}{\theta_b} \frac{t_o(\rho)}{c(\rho)} \cdot \int_0^{\infty} uF(u)[G(u, \ell) + G(-u, \ell)] du d\rho \right\} \quad (38)$$

where

$$F(u) = \left[\sin \frac{u\theta_b}{a} - \frac{u\theta_b}{a} \cos \frac{u\theta_b}{a} \right] / u^2$$

$$G(u, \ell) = I_{\ell N}(1u+a\ell N|\rho) K_{\ell N}(1u+a\ell N|r) e^{iu(x-\sigma'/a)}$$

for $\rho < r$, and the negative sign of ℓ is taken into account in the computer program.

The contribution to the mean or zero harmonic is given by

$$(P_T)_0 = -\rho_f U^2 \left\{ \frac{4a_N}{\pi^2} \int_{\rho} \frac{(1+a^2\rho^2)}{\theta_b} \frac{t_o(\rho)}{c(\rho)} \int_0^{\infty} uF(u) I_0(u\rho) K_0(ur) \cdot \cos[u(x-\sigma'/a)] du d\rho \right\} \quad (39)$$

A numerical procedure for the evaluation of the pressure field due to propeller loading and thickness designated as PFDTLDG is coded in Reference 10, provided the spanwise loading along the blade at the desired frequencies is known through the use of PPEXACT.⁽⁷⁾

Combining Eqs.(28), (34) and (38), the blade frequency pressure at any point on the hull surface can be determined due to the direct propeller

pressure (i.e., propeller fanning effect) and due to the diffraction on account of the presence of the hull.

F. CORRELATIONS OF THEORY WITH EXPERIMENTS

In order to establish the reliability of the procedure for predicting the mean and blade-frequency pressure, the theoretical calculations have been compared with an extensive set of measurements made in Norway. Huse⁽⁴⁾ measured propeller-induced pressures at 34 points on the after-body of a 20-foot tanker model (1:40 scale) of block coefficient 0.80 in the Norwegian Ship Model Experiment Tank. The main particulars of the ship and model are given in Table 1, and of the propeller, in Table 2.

TABLE 1

PARTICULARS OF MODEL 699

	Prototype	Model
Length between perpendiculars	250 m	20.5'
Breadth	42 m	3.45'
Draft	15.24 m	1.25'
Block coefficient	0.80	0.80
Ship speed	17 kt	4.54 ft/sec

TABLE 2

CHARACTERISTICS OF PROPELLER TROOST B-4 SERIES

Number of blades	4
EAR	0.55
Diameter, D, ft	0.671
P/D	0.56
RPM	680
Ship speed, U, ft/sec	4.54
Advance ratio, $J = U/nD$	0.6
$a = \frac{\pi}{J}$	5.236

Relevant geometric characteristics of the Troost B-4 propeller, namely, the ratios of maximum camber to chord length, m_x/c , maximum thickness to chord, t_o/c , of leading edge radius to chord, p_o , of chord to diameter, c/D , and of the pitch to diameter, p/D , at eight radial positions, are given in Table 3.

TABLE 3
PERTINENT GEOMETRIC CHARACTERISTICS OF TROOST B-4 PROPELLER

Radius	m_x/c	t_o/c	p_o	c/D	p/D
0.25	0.0275	0.1700	0.0200	0.223	0.56
0.35	0.0260	0.1300	0.0135	0.256	0.56
0.45	0.0260	0.1030	0.0092	0.282	0.56
0.55	0.0254	0.0820	0.0058	0.301	0.56
0.65	0.0235	0.0620	0.0029	0.308	0.56
0.75	0.0213	0.0488	0.0012	0.298	0.56
0.85	0.0187	0.0391	0.0005	0.259	0.56
0.95	0.0137	0.0313	0.0002	0.171	0.56

The Troost B-4 propeller operates in the wake of Model 699. The harmonic content of the non-dimensional normal velocity on the blade, at 8 equidistant radial positions between propeller hub and tip, is given in Table 4.

TABLE 4
HARMONIC CONTENT OF THE NON-DIMENSIONAL NORMAL VELOCITIES
TO THE PROPELLER BLADE AT VARIOUS RADIAL POSITIONS
 $v_N^{(q)}/U$ (Ref. 12)

r/r_o	$q = 0$		$q = 1$		$q = 2$		$q = 3$		$q = 4$		$q = 5$	
	R	I	R	I	R	I	R	I	R	I	R	I
.25	-.508	0	-.006	-.209	-.073	+.067	0	-.021	-.011	+.015	0	-.013
.35	-.557	0	+.012	-.103	-.058	+.019	+.012	-.025	-.036	+.021	-.002	-.018
.45	-.580	0	+.042	-.043	-.020	+.008	-.028	-.032	-.056	+.023	-.018	-.004
.55	-.592	0	+.057	-.018	-.001	+.012	-.043	-.005	-.065	+.022	-.023	+.010
.65	-.604	0	+.050	-.002	0	+.014	-.027	+.002	-.050	+.017	-.029	+.013
.75	-.574	0	+.036	+.008	-.055	+.005	-.009	+.007	-.029	+.016	-.034	+.009
.85	-.509	0	+.020	+.022	-.116	+.017	-.010	+.007	-.038	+.016	-.024	+.004
.95	-.423	0	0	+.033	-.209	+.032	+.063	-.008	-.083	+.016	-.008	+.002

With the geometric propeller information and harmonic content of the inflow field in which the propeller operates, the steady and time-dependent blade loading and corresponding hydrodynamic forces and moments can be determined by utilizing the numerical procedure⁽⁶⁾ developed and programmed for CDC-6600 or Cyber 176 high-speed digital computer.

The results of the calculations for the steady and unsteady thrust, torque and bearing forces and moments are given in Table 5 (see Figure 4) together with the results for steady state thrust and torque obtained from Troost-charts for comparison.

TABLE 5
SUMMARY OF
HYDRODYNAMIC FORCES AND MOMENTS FOR TROOST B-4 PROPELLER
IN WAKE OF MODEL 699

Steady State		Unsteady (Blade Frequency)
Calculations	Troost Charts	Calculations
$\bar{K}_T = 0.2278$	0.173	$\bar{K}_T = 0.01601$
$\bar{K}_Q = 0.0244$	0.0178	$\bar{K}_Q = 0.001428$
$\bar{K}_{F_y} = 0.00145$		$\bar{K}_{F_y} = 0.00104$
$\bar{K}_{Q_y} = 0.00140$		$\bar{K}_{Q_y} = 0.00125$
$\bar{K}_{F_z} = -0.00174$		$\bar{K}_{F_z} = 0.00102$
$\bar{K}_{Q_z} = -0.00048$		$\bar{K}_{Q_z} = 0.00158$

For the purpose of obtaining the solution of integral equation (4), the hull surface and its positive reflection in the free surface, are subdivided into 392 quadrilaterals as shown in Figures 5 and 6. The coded numerical procedure developed by Hess-Smith is applied, considering the following onset flows: a uniform steady motion of the hull and its image, yielding the source density σ_0 , and the real and imaginary parts of the propeller-induced onset flows which determine the corresponding strengths σ_R and σ_I , respectively.

That the size of the quadrilateral is a crucial factor not only in calculating the hydrodynamic forces and moments but also in evaluating the point pressure and velocity (both oscillatory in character) on the hull has been previously discussed. The selection of proper dimensions for the various

patches considerably increases the number of the required quadrilaterals. This coupled with the complications arising in the calculation of the propeller-induced velocity components makes the numerical approach expensive and rather impractical.

The approach used in this study has therefore not been pursued further. As mentioned earlier, a new study⁽¹³⁾ has been initiated which represents the hull by a doublet distribution whose strength is calculated by the same numerical procedure for the inversion of the integral equation, knowing the propeller velocity potential (a scalar function). This method permits decreasing the mesh-size of the quadrilaterals and increasing the number while still reducing the computer time, and has shown considerable improvement.

However, for this report the calculations have been performed using the quadrilateral arrangement shown in Figures 5 and 6. Out of 392 quadrilaterals, 142 located at the forward part of the hull and away from the propeller are deactivated since the propeller-induced velocities there are negligibly small.

The procedure previously developed in section E is applied to calculate the point pressures at the locations of the transducers shown in Table 6, which are referred to the propeller coordinate system (see Figure 7). The free space pressure (see E-2) is determined by means of the numerical procedure coded in Reference 10 as PFDTLDG and the pressure to the diffraction potential is determined according to the procedure discussed in section E-1. The results of each are presented in Table 7 as are the total pressures with their corresponding magnitudes and phases referred to the hull coordinate system.

The calculations are performed for a propeller-skeg clearance of $b/D = 0.235$ (see Figure 3.6 of Reference 4). It should be noted that the transducer coordinates are determined from the values of ξ/D of Table 4.1 of Reference 4 as follows:

- a) For points on the transom of the hull

$$x/D = (\xi/D \text{ given in Table 4.1 at } b/D = 0.48) + (0.48 - 0.235)$$

- b) For points on the hull skeg

$$x/D = (\xi/D \text{ given in Table 4.1 at } b/D = 0.186) - (0.235 - 0.186)$$

The comparison between predicted and measured magnitudes and phases is presented in Table 8a, and graphically exhibited in Figures 9, 10 and 11 at various hull cross-sections (see Figure 8). The cross-section F-F includes also point pressures from neighboring sections, a fact which explains the abrupt change in the pressure distribution at some points.

The results in Table 8 are presented in pressure coefficient C_p form by defining

$$C_p = \frac{P}{\rho n^2 D^2}$$

where p = magnitude point pressure on hull

ρ = fluid density

D = propeller diameter

n = rps

The ratio of C_p measured to C_p calculated values indicates the degree of correlation between experiment and theory. Note that the phase angles are referred to field point angular position so that the phase angle φ_c as defined in Reference 4 is given by

$$\varphi_c = 270^\circ - 4\epsilon + \varphi_4$$

where

φ_4 = phase angle obtained through the program as $\tan^{-1} \frac{I_m}{Re}$

ϵ = the angular position of the field point given in Table 6.

As was mentioned earlier, the present method where the hull is represented by a distribution of sources smeared over the hull surface has been found uneconomical and has been replaced by a new method where the hull surface is represented by a doublet distribution. Calculations were performed with the same number of quadrilaterals giving a detailed pressure distribution which is graphically exhibited in Figure 9, 10 and 11. On those graphs, both the experimental results and the results using the source distribution are presented as well.

A correlation of theoretical results obtained through the "doublet-approach" with those of experiments is presented in Table 8b. It would be difficult to argue the superiority of the "doublet-approach" over the

"source-distribution" when the comparison is limited to the magnitudes of the point pressures only. When the theoretical phase angles are compared with those of the corresponding experiments, it is definitely concluded that the "doublet-approach" is superior. This result, coupled with the fact that the "doublet-distribution" is more economical by yielding greater accuracy without using excessive computing time, demonstrates the advisability of the "doublet-approach" rather than the "source-distribution."

In Tables 9a and 9b, the values of the so-called "reflection coefficients" are presented as results of theoretical calculations, S_2 , and a combination of measurements and calculations, S_1 . Table 9a presents the results of calculations obtained by means of the "source-approach" whereas Table 9b presents the results obtained by the "doublet-approach."

The "reflection coefficient" defined by Huse⁽⁴⁾ as the "solid boundary factor" actually represents the "image effect" due to the presence of the rigid boundary. It is known that for a rigid boundary of a plane surface of an infinite extent, the reflection coefficient yields a value of $S=2.0$. For a hull surface with a combination of convex, concave, and skeg-type surfaces, it is difficult to assume any suitable value beforehand. It is certainly true that the approximation commonly used by doubling the free-space pressure is valid in cases with a flat, or nearly flat bottom stern in the way of the propeller; however, there are many other instances in which the approximation is very rough and therefore unacceptable. None of the results of Tables 9a and 9b shows any definite trend in this direction.

TABLE 6

TRANSDUCER'S LOCATION IN TERMS OF PROPELLER COORDINATES
WITH PROPELLER-SKEG CLEARANCE AT $b/D = 0.235$

Transducer		x/r_o	r/r_o	φ , radians	or ϵ , deg
C ₁	Transom	0.194 (a)	1.514	0	0
C ₂	Transom	-0.168	1.420	0	0
P ₁	Transom	1.758	2.040	0.197	11.3
P ₂	Transom	0.976	1.860	0.216	12.4
P ₃	Transom	0.194	1.682	0.241	13.8
P ₄	Transom	-0.168	1.600	0.253	14.5
P ₅	Transom	-0.538	1.464	0.278	15.9
P ₇	Transom	0.194	1.970	0.396	22.7
P ₈	Transom	0.194	2.300	0.511	29.3
P ₉	Transom	0.194	2.652	0.588	33.7
P ₁₀	Skeg	-0.684 (b)	1.020	0.153	8.8
P ₁₁	Skeg	-0.722	0.728	0.202	11.6
P ₁₂	Skeg	-1.016	0.772	0.389	22.3
P ₁₃	Skeg	-0.636	0.454	0.328	18.8
P ₁₄	Skeg	-0.576	0.446	2.874	164.7
P ₁₅	Skeg	-0.748	0.760	3.00	171.5
P ₁₆	Skeg	-1.046	0.774	2.899	166.1
S ₁	Transom	1.758	2.040	-0.197	- 11.3
S ₂	Transom	0.976	1.860	-0.216	- 12.4
S ₃	Transom	0.194	1.682	-0.241	- 13.8
S ₄	Transom	-0.168	1.600	-0.253	- 14.5
S ₅	Transom	-0.538	1.464	-0.278	- 15.9
S ₇	Transom	0.194	1.970	-0.396	- 22.7
S ₈	Transom	0.194	2.300	-0.511	- 29.3
S ₁₀	Skeg	-0.684	1.020	-0.153	- 8.8
S ₁₁	Skeg	-0.722	0.728	-0.202	- 11.6
S ₁₂	Skeg	-1.016	0.772	-0.389	- 22.3
S ₁₃	Skeg	-0.636	0.454	-0.328	- 18.8
S ₁₄	Skeg	-0.576	0.446	-2.874	-164.7
S ₁₅	Skeg	-0.748	0.760	-3.00	-171.9
S ₁₆	Skeg	-1.046	0.774	-2.899	-166.1

TABLE 7

POINT PRESSURES AT THE TRANSDUCER'S LOCATION
DUE TO PROPELLER AND DUE TO DIFFRACTION POTENTIAL (Presence of the Hull)

Transd. Quad.	THEORETICAL POINT PRESSURE							
	Due to Propeller		Due to Diffraction		Total Pressure			
	Real	Imaginary	Real	Imaginary	Real	Imaginary	Mag	φ
C ₁ ↑ 12,13	0.26351	0.21697	-0.38404	0.20936	-0.12053	0.42633	0.443	106
C ₂ 14	-0.39576	0.28795	-1.07607	0.61195	-1.47183	0.89990	1.725	149
P ₁ 17	0.06818	0.05127	0.01346	0.02186	0.08164	0.07313	0.110	42
S ₁	0.07047	0.04393	0.02139	0.03280	0.09186	0.07673	0.120	40
P ₂ 19	0.10533	0.09185	-0.00192	0.01741	0.10341	0.10926	0.150	47
S ₂	0.11548	0.02331	0.03533	0.07155	0.15081	0.09486	0.178	32
P ₃ 22	0.00640	0.15652	-0.21569	-0.05289	-0.20929	0.10363	0.234	154
S ₃	0.18377	0.01966	-0.02008	0.27974	0.16369	0.29940	0.341	61
P ₄ 25	-0.25249	-0.03248	-0.66811	-0.37877	-0.92060	-0.41125	1.008	-156
S ₄	0.03646	0.16795	-0.15068	0.72955	-0.11422	0.89750	0.905	97
P ₅ 28	-0.35090	-0.22753	-0.52340	-0.62954	-0.87430	-0.85707	1.224	-136
S ₅	-0.12372	0.17732	0.10715	0.75310	-0.01657	0.93042	0.931	91
P ₆ 31	0.05339	0.06329	-0.00346	-0.01182	0.04993	0.05147	0.070	46
P ₇ 34	-0.02829	0.04017	-0.06663	-0.14383	-0.09492	-0.10366	0.141	-132
S ₇	0.07687	-0.01068	0.11031	0.14798	0.18718	0.13730	0.232	36
P ₈ 33	-0.01605	0.00246	-0.02182	-0.09106	-0.03787	-0.08860	0.096	-113
S ₈	0.03431	-0.00916	0.07820	0.06949	0.11251	0.06033	0.128	28
P ₉ ↓ 32	-0.00676	-0.00767	-0.00564	-0.04532	-0.01240	-0.05299	0.054	-103
P ₁₀ ↑ 44	-0.85609	-0.28651	-0.67435	-0.49409	-1.53044	-0.78060	1.718	-153
S ₁₀	-0.55158	0.31289	0.07075	0.75641	-0.48083	1.06930	1.172	114
P ₁₁ 45	-0.56181	-0.37761	-0.40035	-0.63409	-0.96216	-1.01170	1.396	-133
S ₁₁	-0.25675	0.12826	0.07047	0.71052	-0.18628	0.83878	0.859	103
P ₁₂ 58	-0.10162	-0.43533	-0.08001	-0.02526	-0.18163	-0.46059	0.495	-111
S ₁₂	-0.33155	0.06926	0.14401	0.24039	-0.18754	0.30965	0.362	121
P ₁₃ 46	-0.48863	-0.75591	-0.03826	-0.17861	-0.52689	-0.93452	1.073	-119
S ₁₃	-0.42611	-0.02570	-0.12649	0.27476	-0.55260	0.24906	0.606	156
P ₁₄ 48	-0.65826	0.45380	-0.90732	0.07214	-1.56558	0.52594	1.652	161
S ₁₄	-0.71043	-0.72396	-0.47814	0.01274	-1.18857	-0.71122	1.385	-149
P ₁₅ 53	-0.51649	0.35695	-0.18960	0.13821	-0.70609	0.49516	0.862	145
S ₁₅	-0.74848	-0.10680	-0.15475	-0.25284	-0.90323	-0.35964	0.972	-158
P ₁₆ 62	-0.39088	-0.05751	0.01550	0.06337	-0.37538	0.00586	0.375	179
S ₁₆	-0.11371	-0.26772	-0.11225	-0.30656	-0.22596	-0.57428	0.617	-111
P ₁₇ 63	-0.26621	0.15803						
S ₁₇ ↓	-0.36241	0.05653						

TABLE 8a
CORRELATION OF THEORETICAL RESULTS WITH MEASUREMENTS
SOURCE-APPROACH

Transd. Quad.		COMPARISON OF THEORETICAL AND EXPERIMENTAL RESULTS							$\varphi^{\text{ex}} - \varphi^{\text{th}}$ deg
		Theoretical		Experimental				C_p^{ex}	
		C_p^{th}	φ_c, deg	Upper Boundary	Lower Boundary	C_p^{ex}	φ_c, deg	C_p^{th}	
C_1	12,13	0.00396	16	0.00498	0.00456	0.0048	236	1.21	220
C_2	14	0.01541	59	0.0157	0.0155	0.0156	268	1.01	209
P_1	17	0.00098	-			0.00076	-	0.78	
S_1		0.00107	-	0.00106	0.00054	0.0009	-	0.84	
P_2	19	0.00134	-	0.00084	0.00036	0.00060	-	0.45	
S_2		0.00159	-	0.00275	0.0021	0.0024	-	1.50	
P_3	22	0.00209	8	0.0043	0.0041	0.0042	263	2.00	255
S_3		0.00305	27	0.0063	0.00610	0.0062	287	2.03	260
P_4	25	0.00901	56	0.0115	0.0111	0.0113	275	1.25	219
S_4		0.00808	65	0.0103	0.0099	0.0101	297	1.25	232
P_5	28	0.01094	71	0.0105	0.0095	0.0100	277	0.91	206
S_5		0.00831	65	0.0086	0.0082	0.0084	298	1.01	233
P_6	31	0.00064	-	-	-	-			
P_7	34	0.00126	47	0.0023	0.0021	0.0022	250	1.75	203
S_7		0.00207	37	0.0030	0.0027	0.0028	264	1.35	227
P_8	33	0.00086	40	0.0012	0.0008	0.0010	245	1.16	205
S_8		0.00114	55	0.00155	0.00125	0.0014	310	1.23	255
P_9	32	0.00049		-	-	-			
P_{10}	44	0.01535	82	0.0140	0.0130	0.0135	298	0.88	216
S_{10}		0.01047	59	0.01630	0.01530	0.0156	268	1.49	209
P_{11}	45	0.01247	90	0.01300	0.01200	0.0125	291	1.002	201
S_{11}		0.00767	59	0.01410	0.0131	0.0135	273	1.76	214
P_{12}	58	0.00442	69	0.00470	0.00430	0.0045	273	1.02	204
S_{12}		0.00323	120	0.00520	0.0050	0.0051	322	1.58	202
P_{13}	46	0.00958	75	0.0078	0.0068	0.0075	282	0.78	207
S_{13}		0.00541	141	0.0055	0.0045	0.0050	282	0.93	141
P_{14}	48	0.01475	133	0.0100	0.0095	0.0100	306	0.68	173
S_{14}		0.01237	60	0.0095	0.0085	0.0090	278	0.73	218
P_{15}	53	0.00770	87	0.0100	0.0090	0.0095	273	1.23	186
S_{15}		0.00868	79	0.0090	0.0080	0.0085	283	0.98	204
P_{16}	62	0.00335	145	0.0039	0.0031	0.0035	288	1.04	143
S_{16}		0.00551	103	0.0042	0.0032	0.0037	256	0.67	153

TABLE 8b

CORRELATION OF THEORETICAL RESULTS WITH MEASUREMENTS
DOUBLET-APPROACH

Transd. Quad.	COMPARISON OF THEORETICAL AND EXPERIMENTAL RESULTS							
	Theoretical		Experimental				C_p^{ex}	$\varphi^{ex}-\varphi^{th}$
	C_p^{th}	φ_c, deg	Upper Boundary	Lower Boundary	C_p^{ex}	φ_c, deg	C_p^{th}	deg
C_1 12,13	0.00559	228	0.00498	0.00456	0.0048	236	0.86	8
C_2 14	0.02191	261	0.0157	0.0155	0.0156	268	0.71	7
P_1 17	0.00105	244	-	-	0.00076	-	0.72	-
S_1	0.00089	291	0.00106	0.00054	0.0009	-	1.00	-
P_2 19	0.00032	240	0.00084	0.00036	0.00060	-	1.87	-
S_2	0.00073	308	0.00275	0.0021	0.0024	-	3.28	-
P_3 22	0.00499	230	0.0043	0.0041	0.0042	263	0.84	33
S_3	0.00464	239	0.0063	0.0061	0.0062	287	1.34	48
P_4 25	0.01445	240	0.0115	0.0111	0.0113	275	0.78	35
S_4	0.01190	256	0.0103	0.0099	0.0101	297	0.86	41
P_5 28	0.01741	248	0.0105	0.0095	0.0100	277	0.57	29
S_5	0.01330	269	0.0086	0.0082	0.0084	298	0.63	29
P_6 31	0.00179		-	-	-			
P_7 34	0.00304	226	0.0023	0.0021	0.0022	250	0.72	23
S_7	0.00156	260	0.0030	0.0027	0.0028	264	1.79	4
P_8 33	0.00230	199	0.0012	0.0008	0.0010	245	0.43	46
S_8	0.00047	340	0.00155	0.00125	0.0014	310	2.98	-30
P_9 32	0.00267	173	-	-	-		-	-
P_{10} 44	0.01903	294	0.0140	0.0130	0.0135	298	0.71	4
S_{10}	0.01330	251	0.01630	0.01530	0.0156	268	1.17	17
P_{11} 45	0.01950	284	0.01300	0.01200	0.0125	291	0.64	7
S_{11}	0.01238	271	0.01410	0.0131	0.0135	273	1.09	1
P_{12} 58	0.00899	241	0.00470	0.0043	0.0045	273	0.50	32
S_{12}	0.00262	309	0.0052	0.0050	0.0051	322	1.95	13
P_{13} 46	0.01202	264	0.0078	0.0068	0.0075	282	0.62	18
S_{13}	0.00642	350	0.0055	0.0045	0.0050	282	0.78	-68
P_{14} 48	0.01261	314	0.0100	0.0095	0.0100	306	0.79	-8
S_{14}	0.01490	263	0.0095	0.0085	0.0090	278	0.60	15
P_{15} 53	0.01180	274	0.0100	0.0090	0.0095	273	0.81	-1
S_{15}	0.01390	273	0.0090	0.0080	0.0085	283	0.61	10
P_{16} 62	0.00434	262	0.0039	0.0031	0.0035	288	0.81	26
S_{16}	0.00603	254	0.0042	0.0032	0.0037	256	0.61	2

TABLE 9a

REFLECTION COEFFICIENTS (Solid Boundary Factor)
SOURCE-APPROACH

		$S_1 = \frac{C_p \text{ Experiment}}{C_p \text{ Free-Space Pressure}}$					$S_2 = \frac{C_p \text{ Total}}{C_p \text{ Free-Space Pressure}} \bigg _{\text{Theory}}$		
Trans Quad.		THEORY					EXPER.	$S_1 = \frac{C_p^{\text{exp}}}{C_p^{\text{fsp}}}$	$S_2 = \frac{C_p^{\text{th}}}{C_p^{\text{fsp}}}$
		FREE-SPACE PRESSURE Due to Propeller				Total Pressure C_p	C_p		
		Real	Imaginary	Magni.	C_p				
$\begin{array}{l} C_1 \uparrow 12,13 \\ C_2 \uparrow 14 \\ P_1 \uparrow 17 \\ S_1 \uparrow \\ P_2 \uparrow 19 \\ S_2 \uparrow \\ P_3 \uparrow 22 \\ S_3 \uparrow \\ P_4 \uparrow 25 \\ S_4 \uparrow \\ P_5 \uparrow 28 \\ S_5 \uparrow \\ P_6 \uparrow 31 \\ P_7 \uparrow 34 \\ S_7 \uparrow \\ P_8 \uparrow 33 \\ S_8 \uparrow \\ P_9 \downarrow 32 \end{array}$		0.26351	0.21697	0.34134	0.0030	0.00396	0.0048	1.60	1.32
		-0.39576	0.28795	0.48943	0.0044	0.01541	0.0156	3.54	3.50
		0.06818	0.05127	0.08531	0.00076	0.00098	0.00076	1.00	1.28
		0.07047	0.04393	0.08304	0.00074	0.00107	0.0009	1.21	1.44
		0.10533	0.09185	0.13975	0.00124	0.00134	0.0006	0.50	1.08
		0.11548	0.02331	0.11781	0.00105	0.00159	0.0024	2.28	1.51
		0.00640	0.15652	0.15665	0.00140	0.00209	0.0042	3.00	1.49
		0.18377	0.01966	0.18482	0.00165	0.00305	0.0062	3.75	1.84
		-0.25249	-0.03248	0.25457	0.00227	0.00901	0.0113	4.97	3.96
		0.03646	0.16795	0.17186	0.00153	0.00808	0.0101	6.60	5.28
		-0.35090	-0.22753	0.41826	0.00374	0.01094	0.0100	2.67	2.92
		-0.12372	0.17732	0.21622	0.00193	0.00831	0.0084	4.35	4.30
		0.05339	0.06329	0.08280	0.00074	0.00064	-	-	-
		-0.02829	0.04017	0.04913	0.00044	0.00126	0.0022	5.00	2.86
		0.07687	-0.01068	0.07761	0.00069	0.00207	0.0028	4.05	3.00
		-0.01605	0.00246	0.01624	0.00014	0.00086	0.0010	7.14	6.14
		0.03431	-0.00916	0.03551	0.00032	0.00114	0.0014	4.37	3.56
		-0.00676	-0.00767	0.01022	0.00009	0.00049	-	-	5.44
$\begin{array}{l} P_{10} \uparrow 44 \\ S_{10} \uparrow \\ P_{11} \uparrow 45 \\ S_{11} \uparrow \\ P_{12} \uparrow 58 \\ S_{12} \uparrow \\ P_{13} \uparrow 46 \\ S_{13} \uparrow \\ P_{14} \uparrow 48 \\ S_{14} \uparrow \\ P_{15} \uparrow 53 \\ S_{15} \uparrow \\ P_{16} \uparrow 62 \\ S_{16} \uparrow \\ P_{17} \uparrow 63 \\ S_{17} \downarrow \end{array}$		-0.85609	-0.28651	0.90276	0.00806	0.01535	0.0135	1.67	1.90
		-0.55158	0.31289	0.63415	0.00566	0.01047	0.0156	2.75	1.84
		-0.56181	-0.37761	0.67692	0.00604	0.01247	0.0125	2.06	2.06
		-0.25675	0.12826	0.28700	0.00256	0.00767	0.0135	5.27	2.99
		-0.10162	-0.43533	0.44703	0.00399	0.00442	0.0045	1.13	1.11
		-0.33155	0.06926	0.33870	0.00302	0.00323	0.0051	1.69	1.06
		-0.48863	-0.75591	0.90009	0.00804	0.00958	0.0075	0.94	1.19
		-0.42611	-0.02570	0.42688	0.00381	0.00541	0.0050	1.31	1.42
		-0.65826	0.45380	0.94186	0.00841	0.01475	0.0100	1.19	1.75
		-0.71043	-0.72396	1.01431	0.00906	0.01237	0.0090	0.99	1.36
		-0.51649	0.35695	0.62783	0.00561	0.00770	0.0095	1.69	1.14
		-0.74848	-0.10680	0.75606	0.00675	0.00868	0.0085	1.26	1.28
		-0.39088	-0.05751	0.39509	0.00353	0.00335	0.0035	0.99	0.95
		-0.11371	-0.26772	0.29086	0.00259	0.00551	0.0037	1.43	2.12
		-0.26621	0.15803	0.30958	0.00276	-	-	-	-
		-0.36241	0.05653	0.36679	0.00328	-	-	-	-

TABLE 9b

REFLECTION COEFFICIENTS (Solid Boundary Factor)
DOUBLET-APPROACH

		$S_1 = \frac{C_p \text{ Experiment}}{C_p \text{ Free-Space Pressure}}$				$S_2 = \frac{C_p \text{ Total}}{C_p \text{ Free-Space Pressure}} \bigg _{\text{Theory}}$			
Trans	Quad.	THEORY					EXPER.	$S_1 = \frac{C_p^{\text{exp}}}{C_p^{\text{fsp}}}$	$S_2 = \frac{C_p^{\text{th}}}{C_p^{\text{fsp}}}$
		FREE-SPACE PRESSURE				Total Pressure			
		Real	Imaginary	Magni.	C_p	C_p	C_p		
TRANSOM	C_1 ↑ 12,13	0.26351	0.21697	0.34134	0.0030	0.0056	0.0048	1.60	1.86
	C_2 14	-0.39576	0.28795	0.48943	0.0044	0.0219	0.0156	3.54	4.98
	P_1 17	0.06818	0.05127	0.08531	0.00076	0.0105	0.00076	1.00	1.38
	S_1	0.07047	0.04393	0.08304	0.00074	0.00089	0.0009	1.21	1.20
	P_2 19	0.10533	0.09185	0.13975	0.00124	0.00032	0.0006	0.48	0.25
	S_2	0.11548	0.02331	0.11781	0.00105	0.00073	0.0024	2.28	0.70
	P_3 22	0.00640	0.15652	0.15665	0.00140	0.00499	0.0042	3.00	3.56
	S_3	0.18377	0.01966	0.18482	0.00165	0.00464	0.0062	3.75	2.81
	P_4 25	-0.25249	-0.03248	0.25457	0.00227	0.01445	0.0113	4.98	6.36
	S_4	0.03646	0.16795	0.17186	0.00153	0.01180	0.0101	6.60	7.71
	P_5 28	-0.35090	-0.22753	0.41826	0.00374	0.01741	0.0100	2.67	4.65
	S_5	-0.12372	0.17732	0.21622	0.00193	0.01330	0.0084	4.35	6.89
	P_6 31	0.05339	0.06329	0.08280	0.00074	0.00179	-	-	-
	P_7 34	-0.02829	0.04017	0.04913	0.00044	0.00304	0.0022	5.00	6.91
	S_7	0.07687	-0.01068	0.07761	0.00069	0.00156	0.0028	4.06	2.26
	P_8 33	-0.01605	0.00246	0.01624	0.00014	0.00230	0.0010	7.14	16.43
	S_8 ↓ 32	0.03431	-0.00916	0.03551	0.00032	0.00047	0.0014	4.37	1.47
	P_9	-0.00676	-0.00767	0.01022	0.00009	0.00263	-	-	29.67
SKEG	P_{10} ↑ 44	-0.85609	-0.28651	0.90276	0.00806	0.0190	0.0135	1.67	2.36
	S_{10}	-0.55158	0.31289	0.63415	0.00566	0.0133	0.0156	2.76	2.35
	P_{11} 45	-0.56181	-0.37761	0.67692	0.00604	0.0195	0.0125	2.06	3.23
	S_{11}	-0.25675	0.12826	0.28700	0.00256	0.0124	0.0135	5.27	4.84
	P_{12} 58	-0.10162	-0.43533	0.44703	0.00399	0.0090	0.0045	1.13	2.25
	S_{12}	-0.33155	0.06926	0.33870	0.00302	0.0026	0.0051	1.69	0.86
	P_{13} 46	-0.48863	-0.75591	0.90009	0.00804	0.0120	0.0075	0.93	1.49
	S_{13}	-0.42611	-0.02570	0.42688	0.00381	0.0064	0.0050	1.31	1.68
	P_{14} 48	-0.65826	0.45380	0.94186	0.00841	0.0126	0.0100	1.19	1.50
	S_{14}	-0.71043	-0.72396	1.01431	0.00906	0.0149	0.0090	0.99	1.64
	P_{15} 53	-0.51649	0.35695	0.62783	0.00561	0.0118	0.0095	1.69	2.10
	S_{15}	-0.74848	-0.10680	0.75606	0.00675	0.0139	0.0085	1.26	2.06
	P_{16} 62	-0.39088	-0.05751	0.39509	0.00353	0.0043	0.0035	0.99	1.22
	S_{16}	-0.11371	-0.26772	0.29086	0.00259	0.0060	0.0037	1.43	2.31
	P_{17} 63	-0.26621	0.15803	0.30958	0.00276	0.0038	-	-	1.38
	S_{17} ↓	-0.36241	0.05653	0.36679	0.00328	0.0055	-	-	1.68

G. CONCLUSIONS

The previously developed method for calculating the propeller-induced ship vibration⁽³⁾ has been extended to establish a numerical approach for evaluating the pressure distribution on a hull surface in the presence of the propeller and the free water surface. The hull is represented by a source distribution smeared over the hull surface, whose strength is determined through the solution of a Fredholm integral equation of the 2nd kind in terms of specified propeller-induced velocities. To carry out the numerical solution of the integral equation, the hull surface is subdivided into plane quadrilaterals whose sizes and numbers are very crucial in calculating the propeller-induced hydrodynamic forces and point pressure on the hull. Selection of the proper size for the source panels increases the number of quadrilaterals and this, coupled with complications arising from calculations of the propeller-induced velocity, makes this numerical approach expensive and rather impractical. In fact, the need for accuracy in the numerical procedure is more pronounced in calculating point pressure than in determining the propeller-induced vibratory force since the latter represents the integrated effect of the point pressure over the hull surface. Because of this, a new approach has been developed in which the hull is represented by a doublet distribution. The computing time is reduced to almost half that incurred by the present method although the mesh size has been decreased and the number of quadrilaterals increased. The blade-frequency point pressure is determined by superposing the free-space pressure emanating from the propeller and the pressure due to the diffraction potential. The former is calculated according to the theory and program of Reference 10 whereas the latter is determined through an approximate method developed in Section E of the present study.

A series of calculations was performed to determine point pressures on an M-699 model tanker with $C_B = 0.80$ for which extensive measurements were made at the Norwegian Experimental Tank. The correlation between experimental values and those predicted by this proposed method shows a tolerable discrepancy in magnitude of pressure signals but the values of the corresponding phases show very poor agreement. This fact is attributed mainly to the size and number of quadrilaterals which affect the solution of the integral

equation and, consequently, the values of the vibratory forces and point pressures on the hull surface, all of which have not yet converged to their final values. This approach has been suspended as being expensive and impractical.

The new method suggested in which the hull is represented by a doublet distribution rather than a source distribution is a decided improvement. In fact, the doublet distribution is superior to the source approach not only because it is a more economical approach but also by allowing the use of a larger number of quadrilaterals, the results are more accurate, showing a decisive improvement in phases and moderate improvement in magnitude of the pressure points compared to the corresponding experimental values.

As for the "reflection coefficient" which presents the effect of the image due to the presence of a rigid wall, it is difficult to discern any definite trend or to draw any conclusion. The commonly used approximation of doubling the free space pressure does not seem to be valid in this set of calculations. Conclusions cannot be drawn at this stage until additional calculations are performed and compared with experiments.

It would seem unlikely that a reflection factor greatly in excess of 2.0 should be obtained except possibly near the aft extremity of the skeg. In any event, numerical procedures such as advanced here should really be compared for cases in which an independent method can be employed. As the Green's function for a spheroid is known it is recommended that the program be employed for that case and comparisons made with the outcome of the theory for a spheroid in the presence of a single rotating source. Only in this way can definitive information be secured regarding the maximum panel size permitted to achieve a requisite accuracy.

H. REFERENCES

1. Breslin, J.P. and Eng, K., "A Method for Computing Propeller-Induced Vibratory Forces on Ships," *First Conference on Ship Vibration*, Stevens Institute of Technology, 25 January 1965.
2. Vorus, W.S., "A Method for Analyzing the Propeller-Induced Vibratory Forces Acting on the Surface of a Ship Stern," Transactions, SNAME, Vol.82, 1974.
3. Tsakonas, S. and Valentine, D., "Theoretical Procedure for Calculating the Propeller-Induced Hull Forces," Report SIT-DL-79-9-1979, Stevens Institute of Technology, 1979.
4. Huse, E., "The Magnitude and Distribution of Propeller-Induced Surface Forces on a Single-Screw Ship Model," Norwegian Ship Model Experiment Tank Publication No.100, December 1968.
5. Hess, J.L. and Smith, A.M., "Calculations of Non-Lifting Potential Flow About Arbitrary Three-Dimensional Bodies," Douglas Aircraft Division, Report No. E.S. 40622, 15 March 1962.
6. Tsakonas, S., Jacobs, W.R., and Ali, M.R., "Propeller Blade Pressure Distribution Due to Loading and Thickness Effect," Report SIT-DL-76-1869, April 1976; J. Ship Research, Vol.23, No.2, June 1979.
7. Tsakonas, S., Jacobs, W.R., and Ali, M.R., "Documentation of a Computer Program for the Pressure Distribution, Forces and Moments on Ship Propellers in Hull Wakes," Davidson Laboratory Report in Four Volumes, SIT-DL-76-1863.
8. Jacobs, W.R. and Tsakonas, S., "Propeller Loading Induced Velocity Field by Means of the Unsteady Lifting Surface Theory," J. Ship Research, Vol.17, No.3, Sept. 1973.
9. Jacobs, W.R. and Tsakonas, S., "Propeller-Induced Velocity Field Due to Thickness and Loading Effects," J. Ship Research, Vol.19, No.1, March 1975.
10. Tsakonas, S., Jacobs, W.R., and Ali, M.R., "Documentation of a Computer Program for the Pressure Field Generated by a Propeller in a Variable Inflow," Davidson Laboratory Report, SIT-DL-77-1910, May 1977.
11. Jacobs, W.R., Valentine, D.T., and Ali, M.R., "Documentation of a Computer Program for the Velocity Field Induced by a Marine Propeller; User's Manual," Report SIT-DL-78-9-2042, December 1978.

12. Huse, E., "An Experimental Investigation of the Dynamic Forces and Moments on One Blade of a Ship Propeller," Proceedings, Symposium on Testing Techniques in Ship Cavitation Research, Trondheim, 1967.
13. Tsakonas, S., Breslin, J.P., and Liao, P., "Correlation of Theoretical and Experimental Non-Cavitating, Propeller-Induced Vibratory Hull Forces and Point Pressures," Report SIT-DL-80-9-2162, December 1980. [In preparation.]

APPENDIX
EVALUATION OF $\Lambda^{(\bar{n})}(z)$ AND $\Lambda_1^{(\bar{n})}(z)$ FUNCTIONS

$$(1) \quad \Lambda^{(\bar{n})}(z) = \int_0^\pi \Theta(\bar{n}) e^{-iz \cos \theta} \sin \theta \, d\theta$$

a) Birnbaum distribution

$$\Lambda^{(1)}(z) = \frac{1}{\pi} \int_0^\pi \cot \frac{\theta}{2} e^{-iz \cos \theta} \sin \theta \, d\theta = J_0(z) - iJ_1(z)$$

$$\begin{aligned} \Lambda^{(\bar{n}>1)}(z) &= \frac{1}{\pi} \int_0^\pi \sin(\bar{n}-1)\theta \sin \theta e^{-iz \cos \theta} \, d\theta \\ &= \frac{(-i)^{\bar{n}-2}}{2} \left[J_{\bar{n}-2}(z) + J_{\bar{n}}(z) \right] \end{aligned}$$

b) "Roof-top" distribution (\bar{a} mean lines)

$$\begin{aligned} \Lambda^{(1)}(z) &= \int_0^{\cos^{-1}(1-2\bar{a})} e^{-iz \cos \theta} \sin \theta \, d\theta \\ &\quad + \int_{\cos^{-1}(1-2\bar{a})}^\pi \frac{(1+\cos \theta)}{2(1-\bar{a})} e^{-iz \cos \theta} \sin \theta \, d\theta \\ &= e^{-iz} \left\{ \frac{i}{z} + \frac{1}{2(1-\bar{a})z^2} \left[e^{i2\bar{a}z} - e^{i2z} \right] \right\} \end{aligned}$$

$$(\text{For } \bar{a} = 1, \Lambda^{(1)}(z) = \frac{2 \sin z}{z}.)$$

$$\Lambda^{(\bar{n}>1)}(z) = 0$$

c) Sine series distribution

$$\begin{aligned} \Lambda^{(n)}(z) &= \frac{1}{\pi} \int_0^\pi \sin n\theta \sin \theta e^{-iz \cos \theta} \, d\theta \\ &= \frac{(-i)^{\bar{n}-1}}{2} \left[J_{\bar{n}-1}(z) + J_{\bar{n}+1}(z) \right] \end{aligned}$$

$$(2) \quad \Lambda_1^{(\bar{n})}(z) = \int_0^\pi \Theta(\bar{n}) \sin\theta \cos\theta e^{-iz\cos\theta} d\theta$$

a) Birnbaum distribution

$$\Lambda_1^{(1)}(z) = \frac{1}{2} [J_0(z) - J_2(z)] - iJ_1(z)$$

$$\Lambda_1^{(\bar{n}>1)}(z) = \frac{(-i)^{\bar{n}+1}}{4} [J_{\bar{n}-3}(z) - J_{\bar{n}+1}(z)]$$

b) "Roof-top distribution (\bar{a} mean lines)

$$\Lambda_1^{(1)}(z) = e^{-iz} \left\{ \frac{i}{z} + \frac{1}{z^2} + \frac{1}{z^2(1-\bar{a})} \left[\frac{(1-2\bar{a})}{2} - \frac{i}{z} e^{i2\bar{a}z} + \left(\frac{1}{2} + \frac{i}{z} \right) e^{i2z} \right] \right\}$$

$$(\text{For } \bar{a} = 1, \Lambda_1^{(1)}(z) = \frac{i2}{z} (\cos z - \frac{\sin z}{z}).)$$

c) Sine series distribution

$$\Lambda_1^{(\bar{n})}(z) = \frac{(-i)^{\bar{n}+2}}{4} [J_{\bar{n}-2}(z) - J_{\bar{n}+2}(z)]$$

It is to be noted that the values for negative argument, i.e., $\Lambda^{(\bar{n})}(-z)$ and $\Lambda_1^{(\bar{n})}(-z)$, are the conjugates of the values given above.

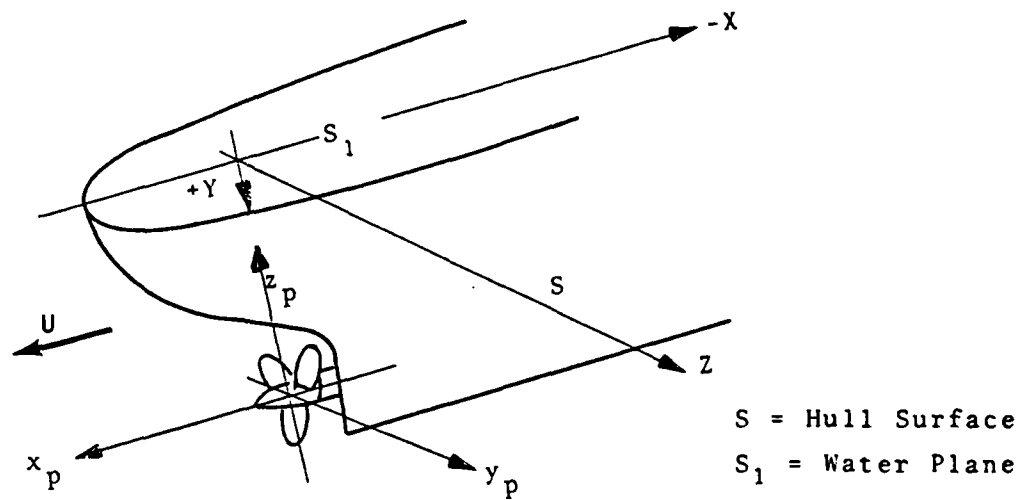


FIGURE 1. PROPELLER-SERIES 60 HULL ARRANGEMENT WITH
COORDINATE AXES WITH RESPECT TO PROPELLER
AND TO HULL

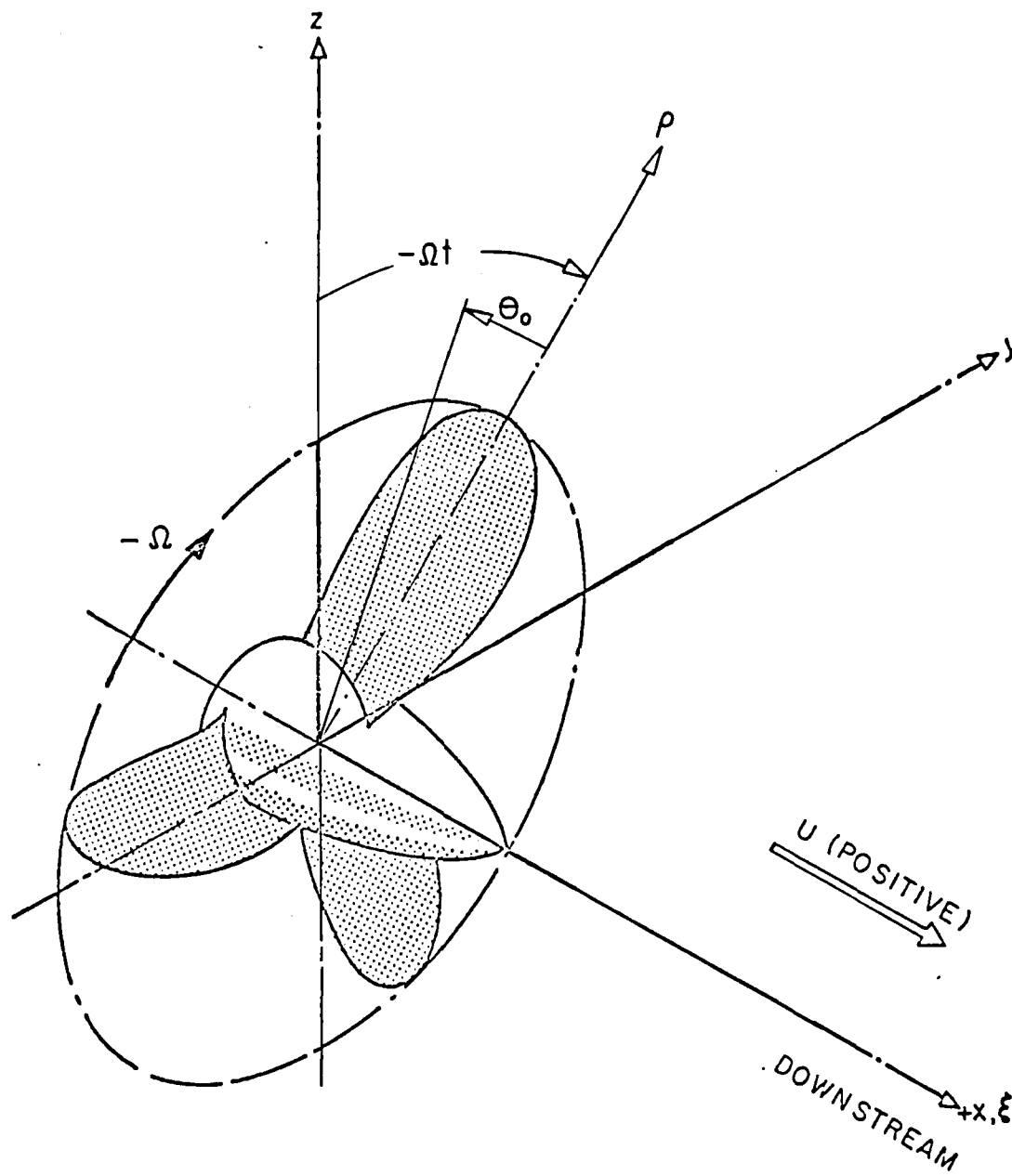


FIG. 2 PROPELLER COORDINATE SYSTEM

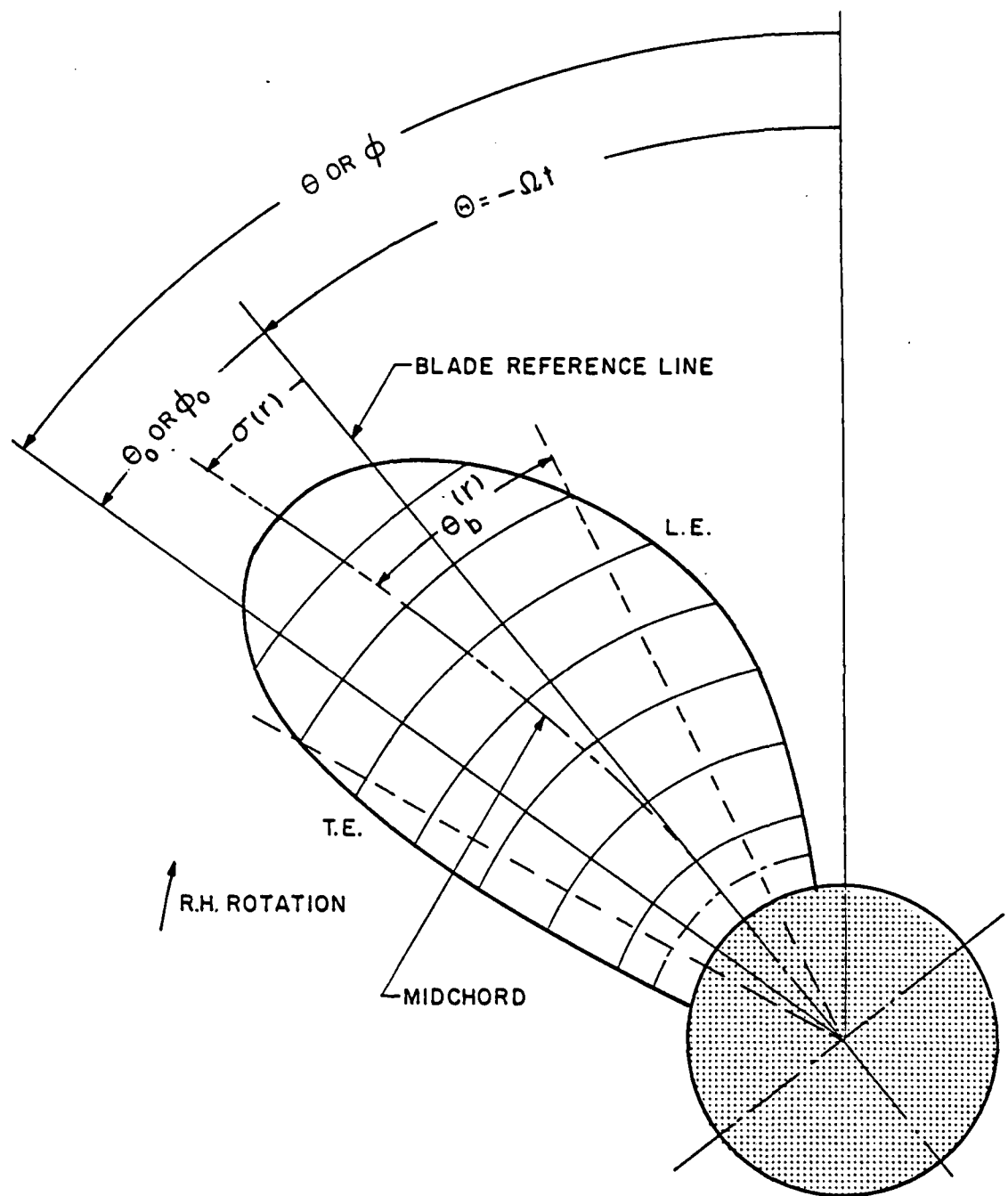


FIG. 3 DEFINITIONS OF ANGULAR MEASURES

NOTE: THE BLADE REFERENCE LINE IS THAT CONNECTING THE SHAFT CENTER WITH THE MIDPOINT OF THE CHORD AT THE HUB

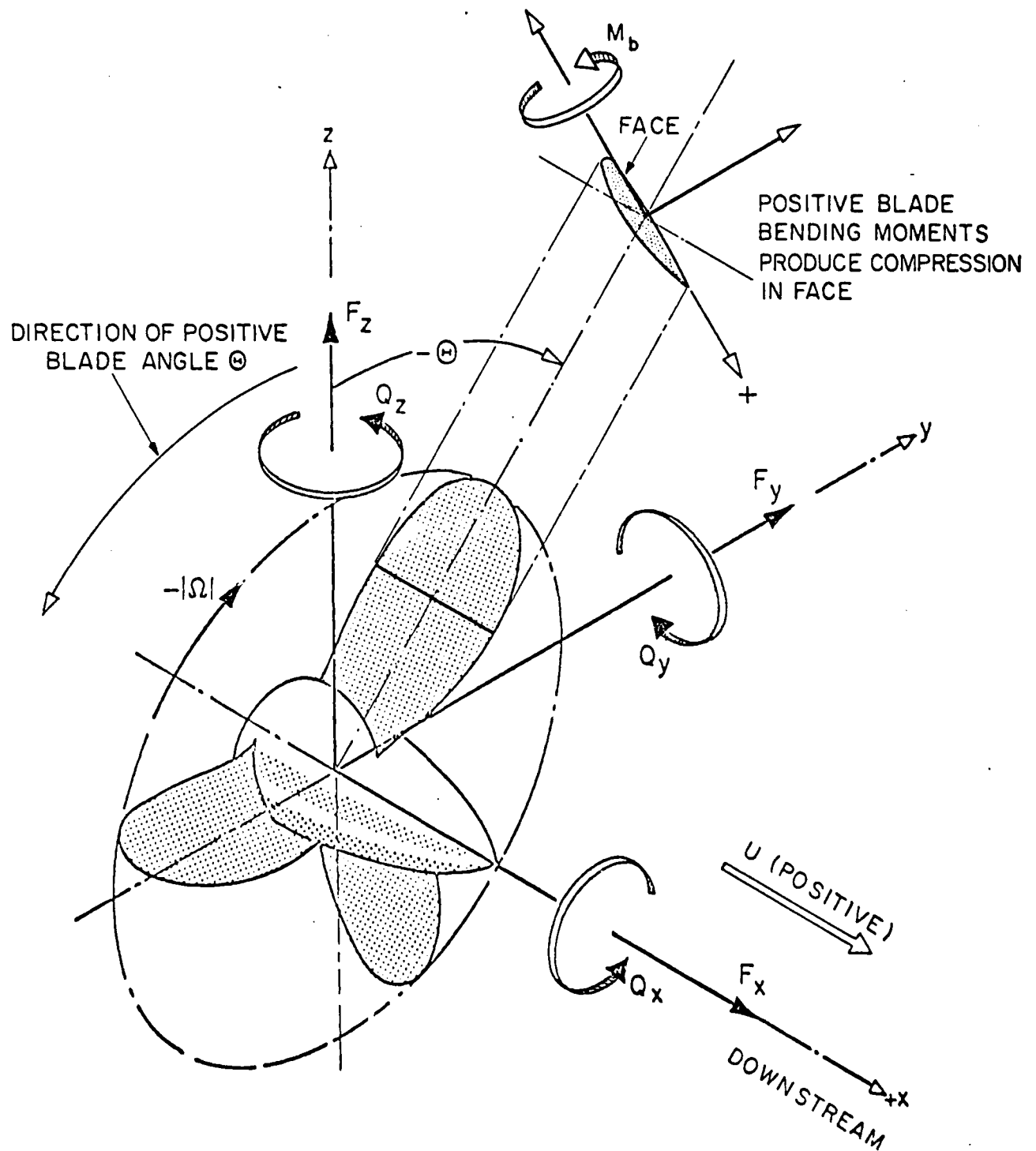


FIG. 4 RESOLUTION OF FORCES AND MOMENTS

R-2140

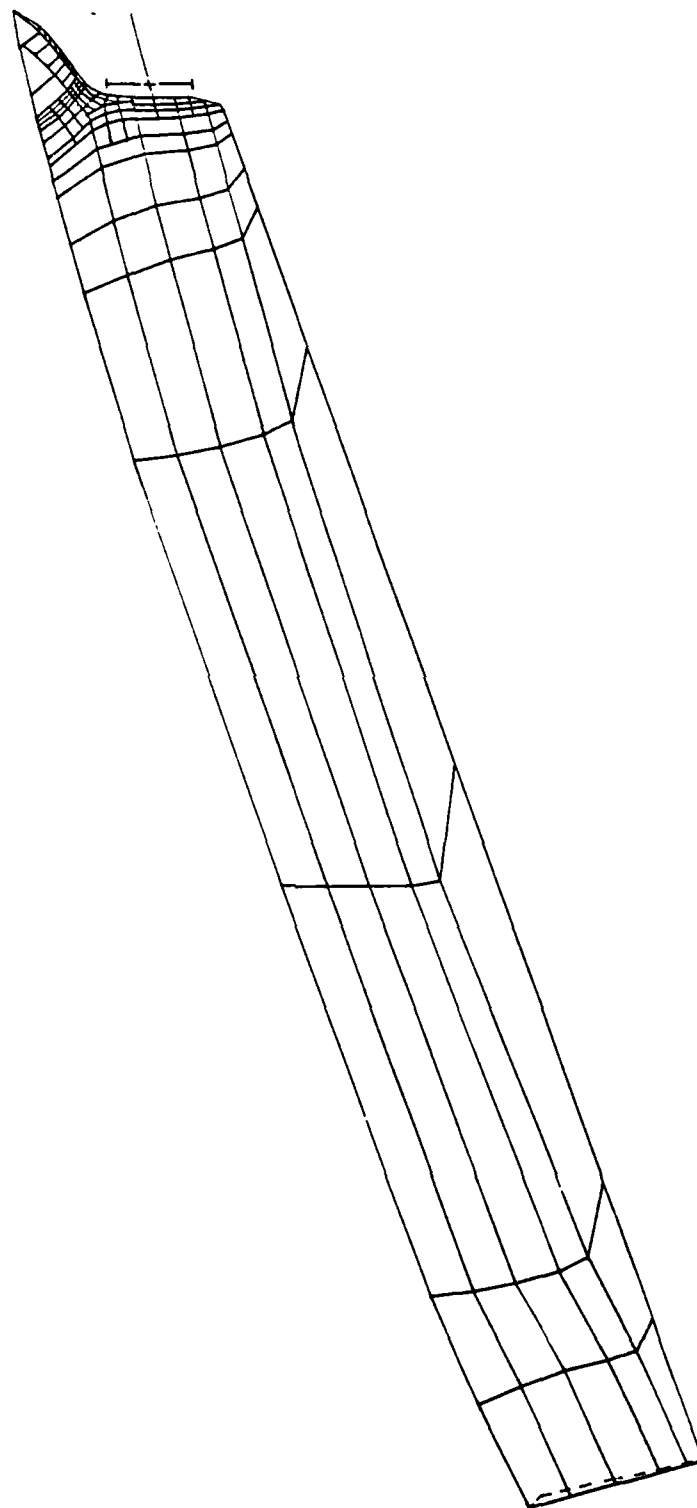


FIG. 5 SOURCE PANEL DISTRIBUTION ON MODEL M-699

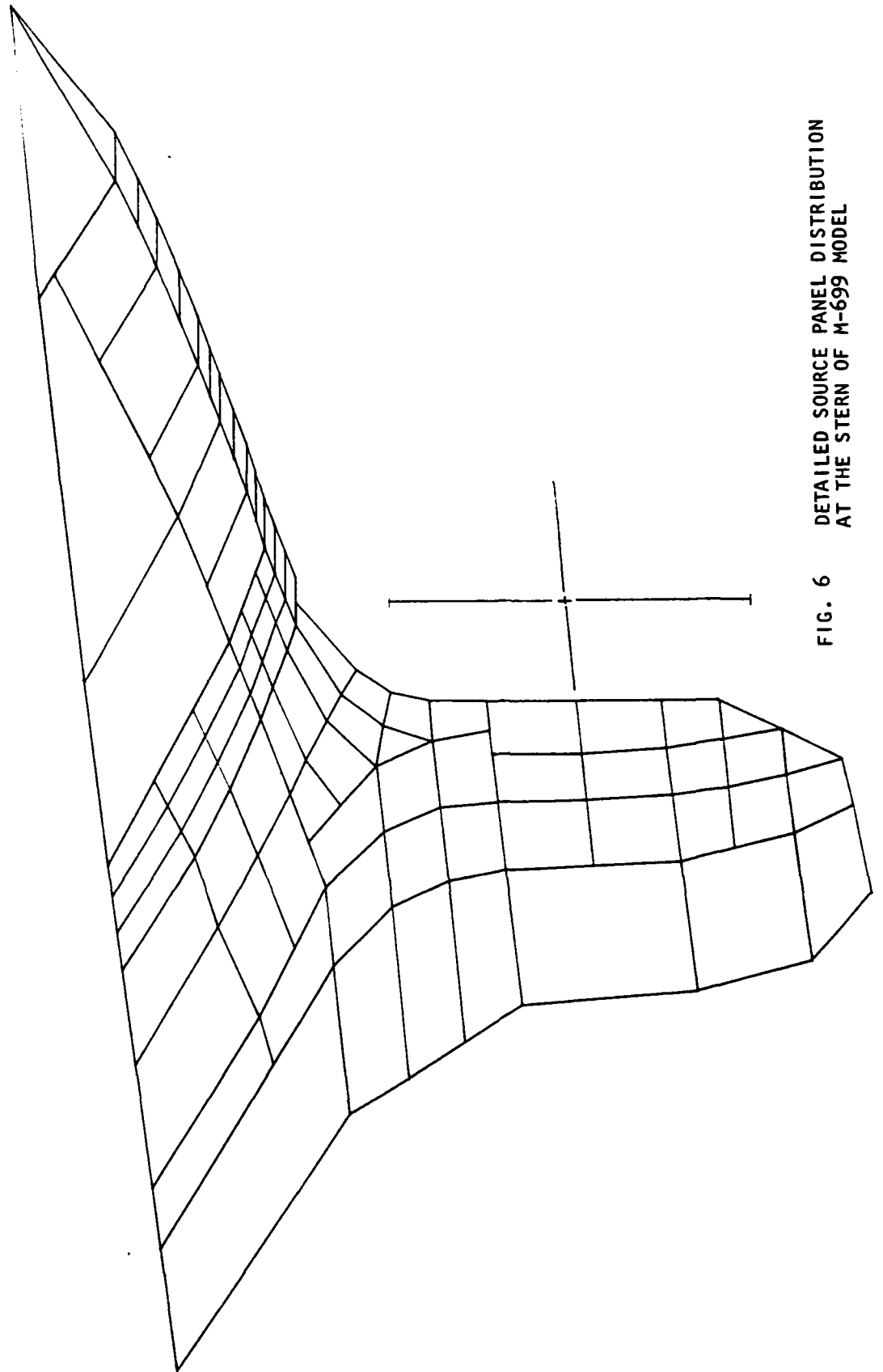


FIG. 6 DETAILED SOURCE PANEL DISTRIBUTION
AT THE STERN OF M-699 MODEL

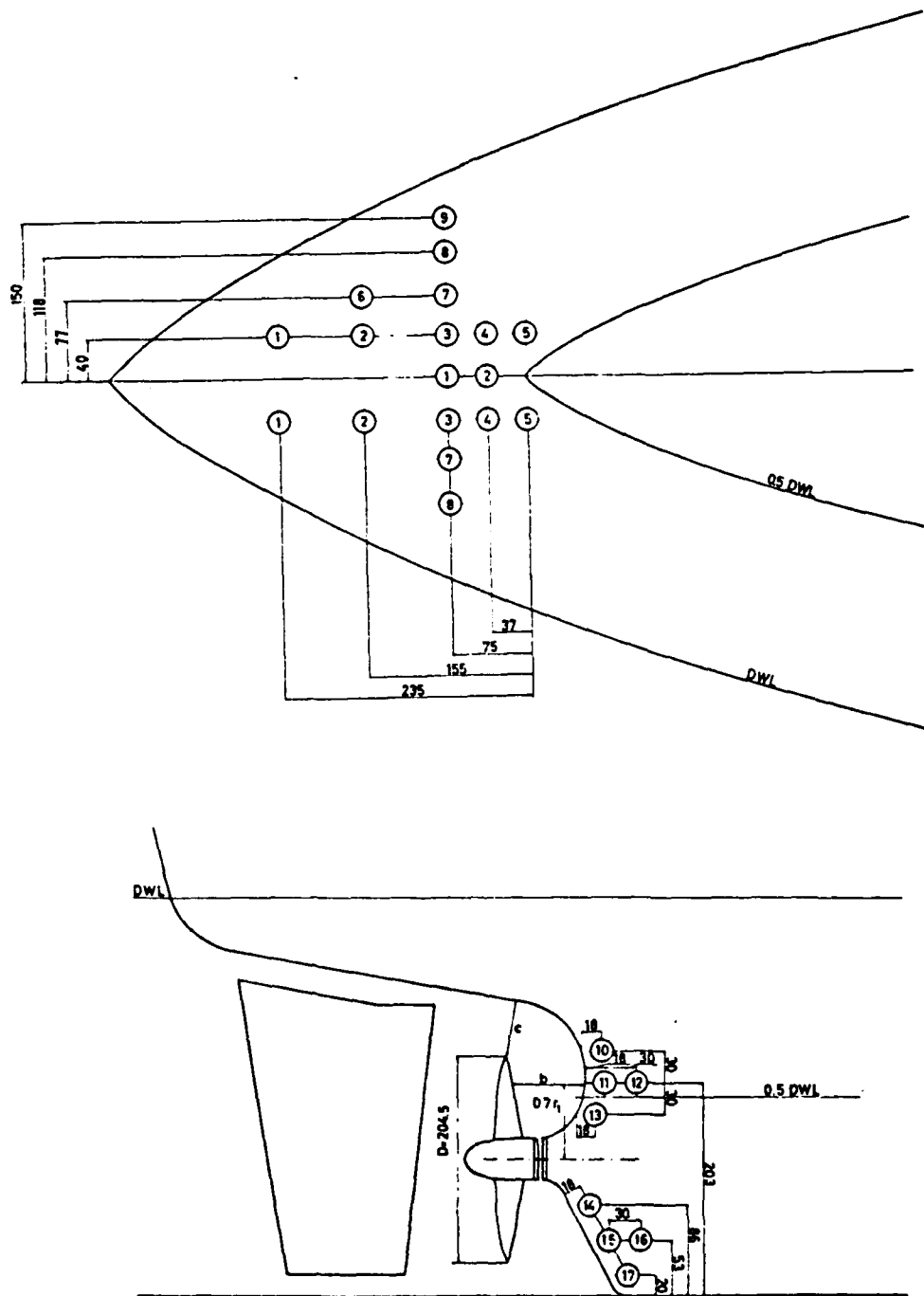


FIG. 7. Transducer positions on skeg and transom, projected [Fig.3.6 in vertical and horizontal plane respectively. Numbers of Ref. 4] in circles are position identifications. Distances are in millimeters on model.

R-2140

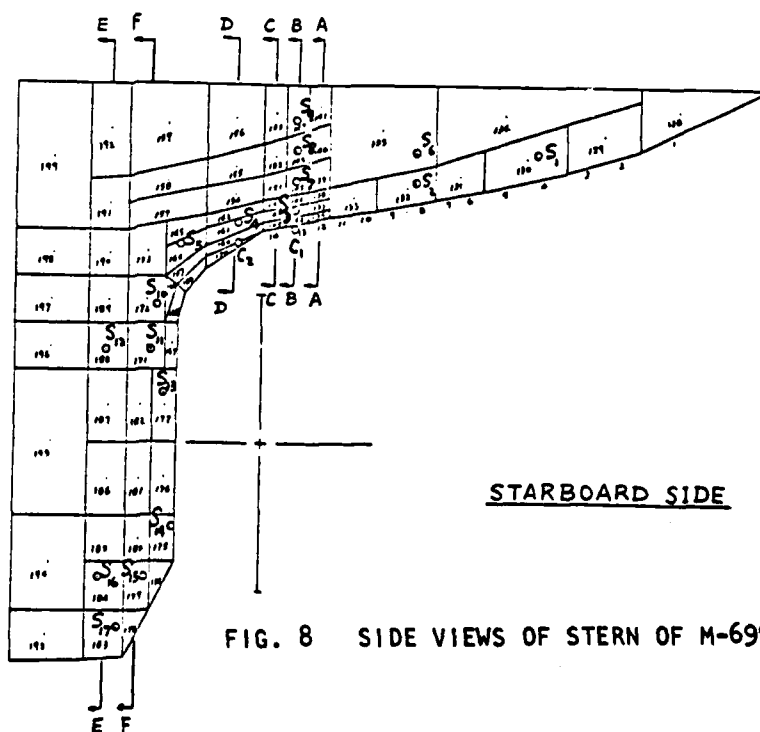
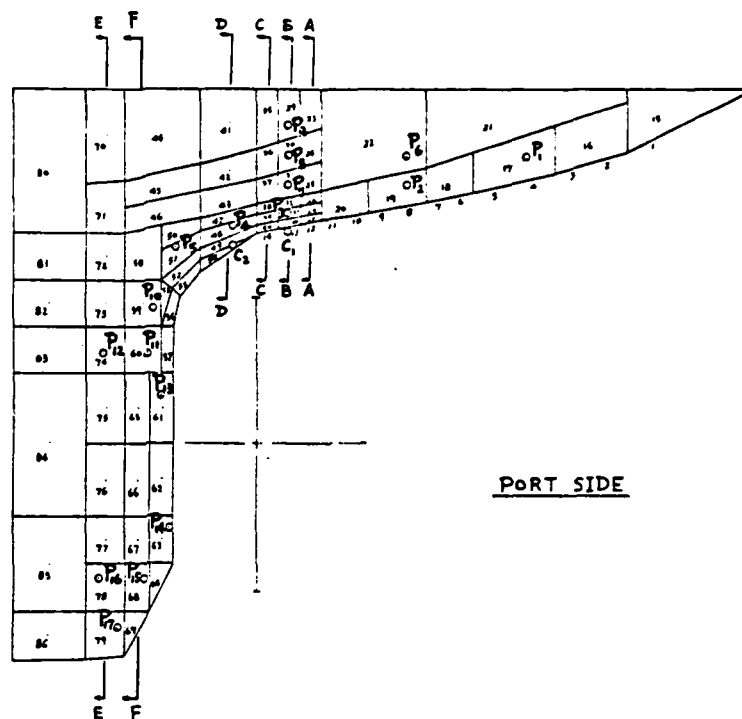


FIG. 8 SIDE VIEWS OF STERN OF M-699 MODEL

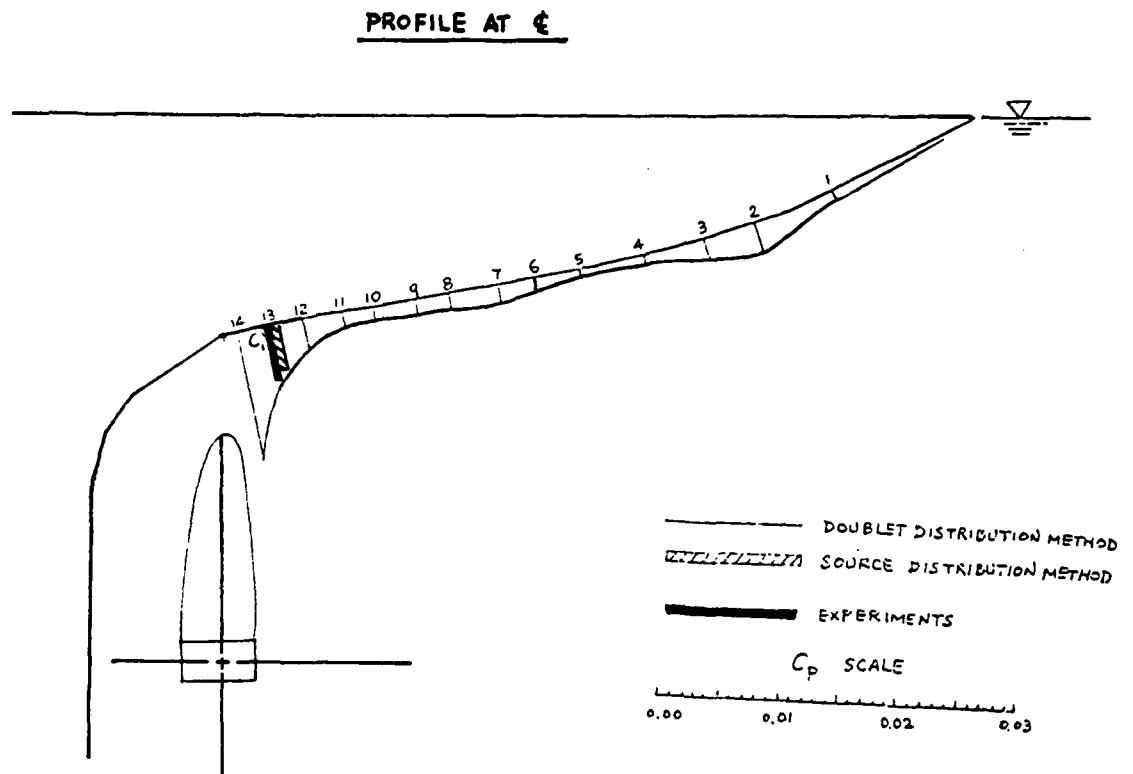


FIG. 9 CORRELATION OF MEASURED AND CALCULATED PRESSURES
(BOTH WITH SOURCE DISTRIBUTION AND DOUBLET
DISTRIBUTION). PROFILE AT CENTERLINE.

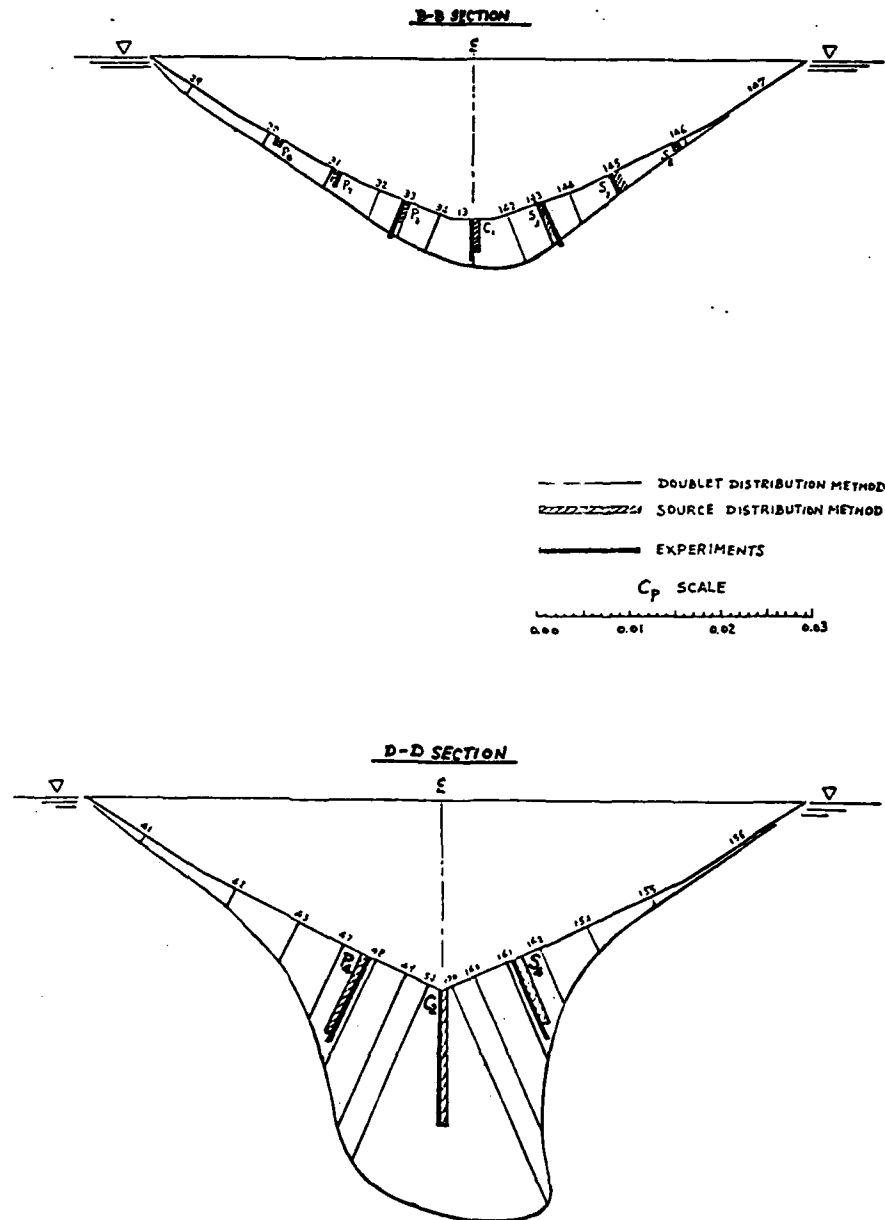


FIG. 10 CORRELATION OF MEASURED AND CALCULATED PRESSURES
(BOTH WITH SOURCE DISTRIBUTION AND DOUBLET
DISTRIBUTION) AT SECTIONS B-B AND D-D.

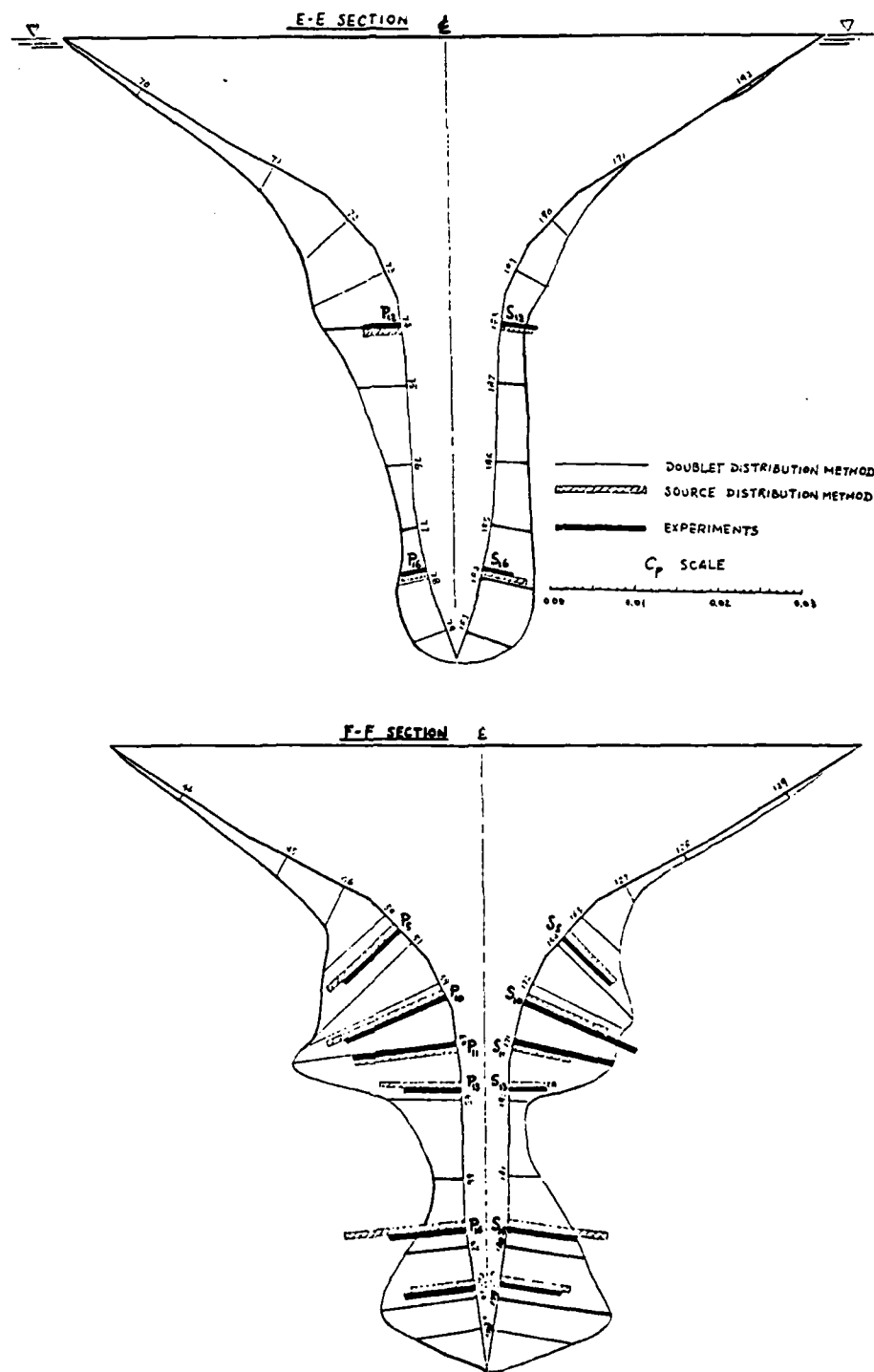


FIG. 11 CORRELATION OF MEASURED AND CALCULATED PRESSURES
(BOTH WITH SOURCE DISTRIBUTION AND DOUBLET
DISTRIBUTION) AT SECTIONS E-E AND F-F.